Chapter 7

Multilayer barrier for particle encapsulation

The permeation barrier film is made by plasma-enhanced chemical vapor deposition (PECVD) from hexamethyldisiloxane and oxygen such that the radio-frequency (RF) power that is fed into the plasma is varied from high to low to high during the deposition. This variation has four desired effects on the film's properties. The effects are: (1) the barrier conformally coats substrate roughness, profiles, and particulate contaminants on the substrate; (2) the barrier has ultralow permeability for water, which ensures a long operating life of the OLED device that the barrier protects; (3) the mechanical stress built into the barrier by deposition does not exceed critical values that would cause delamination; (4) the barrier is flexible. These features, of barrier deposition and of barrier properties, combine to a permeation barrier with unique properties. This chapter describes this multilayer barrier film.

7.1 Three layer barrier structure

From the studies of particle encapsulation in chapter 6 a three layer barrier film is identified for use in encapsulation of OLEDs. The three layers are deposited at three different radio frequency power levels. Figure 7.1 provides a schematic representation of the three layer structure:

1. The bottom layer deposited at high deposition power.

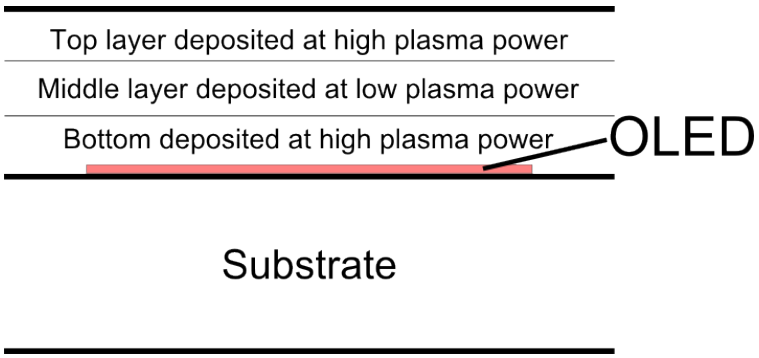

Figure 7.1: Schematic of a three layer barrier structure protecting an OLED. The bottom and top layers are deposited at high radio frequency (RF) power. The middle layer is deposited at low RF power.

2. The middle layer deposited at low deposition power.

3. The top layer deposited at high deposition power.

The deposited film meets the functional requirements during the barrier's operational lifetime that are described below.

7.1.1 Conformable coating

The bottom layer provides adhesion and keeps the chimney alongside a particle small(chapter 6). The bottom layer also keeps the stress within critical bounds. The radio frequency deposition power determines the conformal nature of the deposited layer. The lower the deposition power, the longer is the surface diffusion length of the growth species. As a result, a low deposition power yields a conformal layer. Hence a middle lower power and higher pressure is used to conformally coat the device even when it is rough or has particles on its surface. The top layer is deposited over the middle to provide protection from water permeation and cracking. Figure 7.2a schematically shows how the low RF power hybrid layer coats a substrate with a rough surface. Figure 7.2b schematically shows how such a layer coats the edge steps associated with a patterned OLED. Figure 7.2c shows, again schematically, how the hybrid layer envelopes a dust particle that accidentally settled on the OLED. Figure 7.2d is identical to figure 7.2c but illustrates a bezel around the OLED.

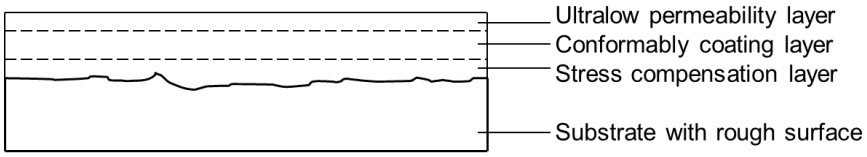

(a) Hybrid barrier film that conformably coats a rough substrate.

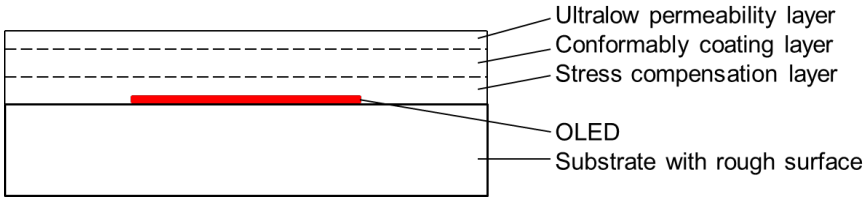

(b) Hybrid barrier film that conformably coats an OLED fabricated features on a rough substrate.

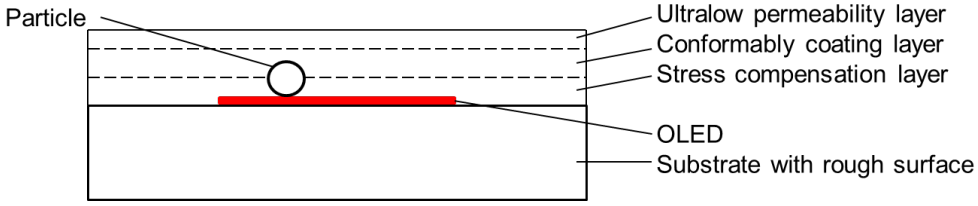

(c) Hybrid barrier film conformably coating an OLED with a contaminant particle.

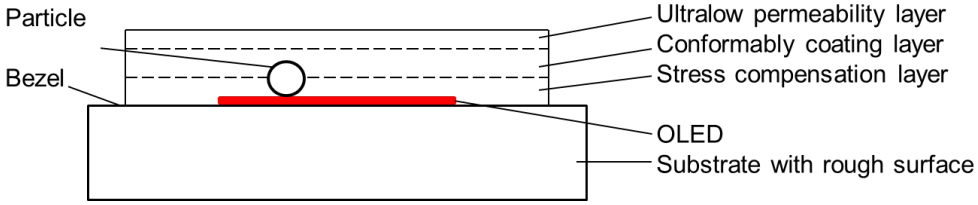

(d) Hybrid barrier film coating an OLED with a distinct bezel around the OLED.

Figure 7.2: Functions of a three layer hybrid film that encapsulates OLEDs

.

7.1.2 Ultralow permeation of water

The flux of water molecules through a defect-free hybrid barrier and into an OLED is proportional to the diffusion coefficient D and solubility S of water in the layer as discussed in chapter 4. Figure 7.3 shows how D depends on the RF deposition power with which the layer was made. D was obtained by monitoring the evolution of mechanical stress barrier layer/silicon wafer couples as a function of time at 100 °C and 100% relative humidity. The D data of figure 7.3 apply to one specific composition of the gaseous precursors used to deposit the barrier as given in table 3.2.

While the standard layer given in table 3.2 already has a very low diffusion coefficient, even lower values are obtained when the RF deposition power is increased. Therefore, to reduce the flux

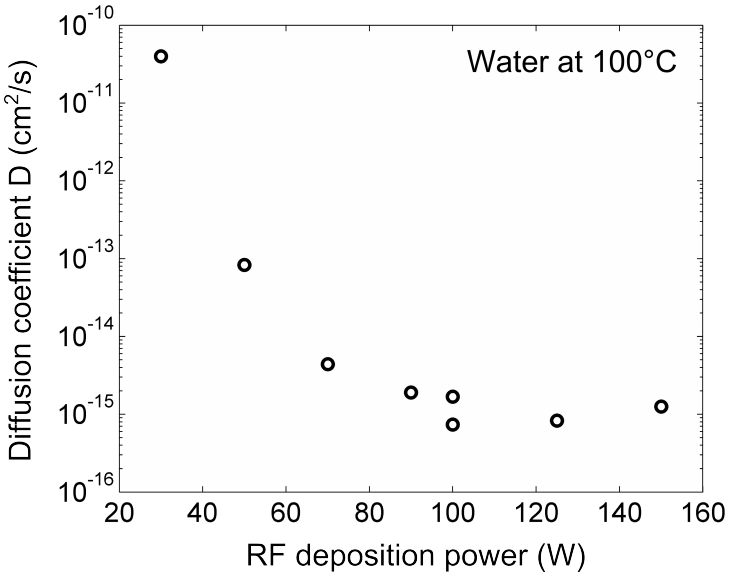

Figure 7.3: Diffusion coefficient of water at 100 °C into the hybrid barrier film, as a function of the radio frequency plasma power used in deposition. The diffusion coefficient is extracted from stress evolution of barrier layer/silicon wafer couples (chapter 4).

of water molecules to the OLED to its lowest achievable value for a given barrier film thickness, in the three layer structure, the top layer is deposited at high RF power. This third layer is shown schematically as the top layer in figure 7.1 and figure 7.2.

Example of a structure for achieving ultralow permeation: Figure 7.4 shows a schematic cross section of a hybrid barrier film on an OLED that is fabricated on a substrate. Figure 7.5 schematically illustrates the permeation of water into the three layer barrier. The concentration of water in the barrier is plotted against depth from the surface of the barrier at $x = 0$. The OLED lies at x =4 μm. The steep profile between the surface and 1 μm depth reflects the very low diffusion coefficient D in the top layer deposited at high RF power. The extremely shallow profile between 1 μm and 3 μm reflects the high D of the layer deposited at low RF power. The high power layer between 3 μm and 4 μm has higher diffusion coefficient than the top layer resulting in a shallow profile as well. Note that all permeabilities are very low, as they correspond to diffusion coefficients of water, at 100 °C, in the range of 10^{-16} cm^2/sec to 10^{-13} cm^2/sec as shown in figure 7.3. A more detailed evaluation below will show that $D = 10^{-16}$ cm^2/sec at 100 °C translates to an OLED lifetime of 20 years at 30 °C 100% relative humidity when the OLED is protected by a single conformal 1 μm thick barrier.

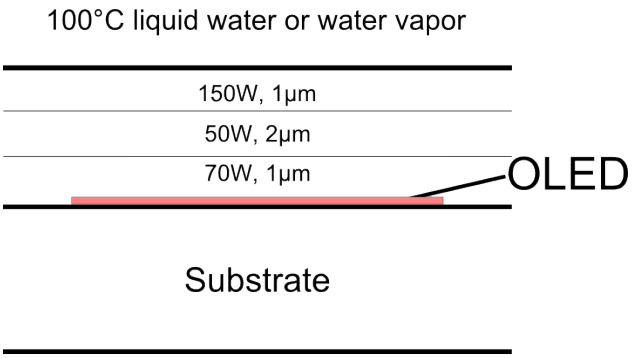

Figure 7.4: Schematic cross section of an OLED display, showing a substrate, an OLED, a conformable hybrid barrier film deposited at three settings of radio frequency powers. The bottom, middle and top layers are deposited at 70 W, 50 W and 150 W respectively. The inscription at the top shows typical conditions for accelerated test of water permeation, 100 °C in liquid water or steam.

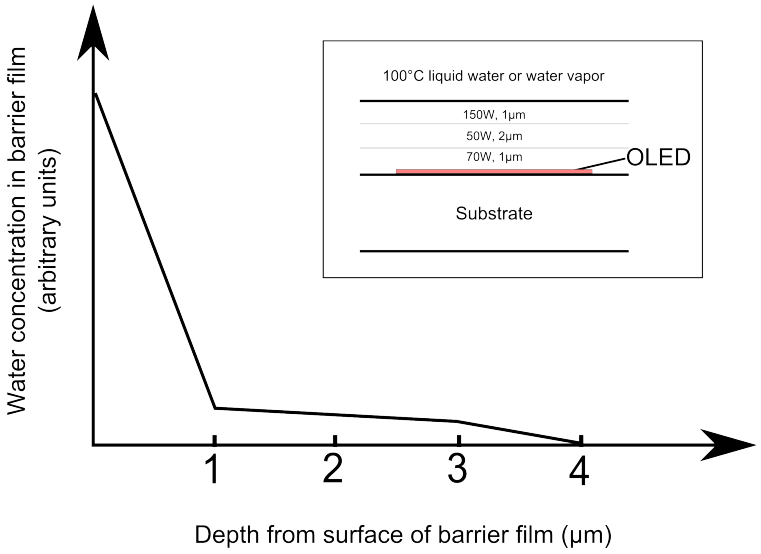

Figure 7.5: Water concentration profile illustration after the water concentration in the barrier film described in figure 7.4 has reached steady state. The layer that limits permeation is the top high power layer. As a result the concentration of water drops most in the top layer between $x = 0$ and 1 µm.

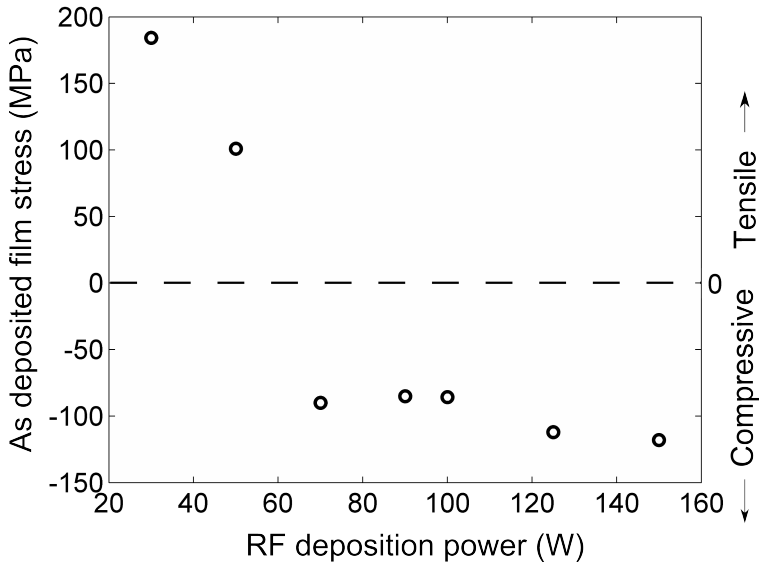

Figure 7.6: Built-in mechanical stress of single-layer hybrid barrier films as function of the radio frequency power.

7.1.3 Minimal barrier stress

The mechanical force per unit length exerted by the barrier film on the substrate is the product of the average mechanical stress in the barrier film and the barrier thickness. This is called surface stress. Changing the RF power from high to low to high as the permeation barrier is deposited keeps the mechanical stress in the permeation barrier film at the low values that are required to prevent layer delamination. Figure 7.6 shows the measured mechanical stress in barrier layers as a function of RF power. It is seen that layers deposited at low RF power are under tensile (positive by definition) built-in stress, while layers deposited at high power are under compressive (negative) stress.

Therefore, depositing the permeation barrier in the high-power to low-power to high-power sequence as described above results in stress compensation. This is illustrated in figure 7.7. The middle layer deposited at low RF power is required for conformal coating over particles and has tensile surface stress. The middle layer would delaminate during the deposition due to poor adhesion and excessive tensile stress if deposited directly on the OLED substrate. To improve adhesion and prevent the build-up of tensile stress, the deposition is started with a bottom high-power barrier layer that has compressive stress. This reduces the tensile stress which otherwise would be very high and cause delamination during deposition.

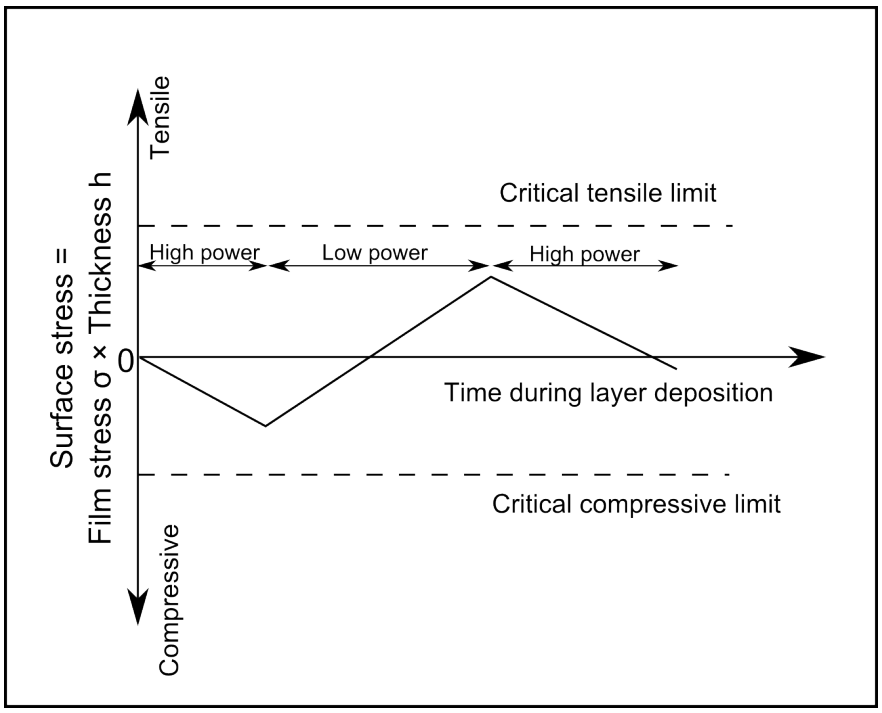

Figure 7.7: The evolution of the $surfacestress = stress \times thickness$ as a function of film deposition time in a three layer film over time is shown. The barrier film is designed to stay within critical limits of tensile and compressive stress during its deposition and use, to prevent delamination of the film.

The film of Figure 7.7 is deposited in the same sequence as implied in figures 7.1, 7.2 and 7.4. The two dashed horizontal lines show the critical surface stresses, tensile and compressive, at which the hybrid barrier film would delaminate. The curve with two slopes shows the development of film stress during the film's deposition. The initial deposition at high RF power builds a layer with compressive stress (see values Figure 6). The following deposition at low RF power builds a tensile stress. The subsequent top layer deposition at high power, by adding a layer with compressive stress, reduces the total built-in stress of the film. During the entire period of deposition the total stress in the film is held in a band bounded by the critical values at which the film would delaminate. A similar consideration applies to the surface stress during the operating life of the OLED that the film protects.

During operation the hybrid barrier film is exposed to water vapor, and water molecules diffuse into the hybrid layer. This uptake of water swells the hybrid layer. The ensuing expansion of the hybrid layer is constrained by the substrate to which the layer is attached. This constraint causes the stress in the hybrid layer to become more compressive during the operating life of the OLED

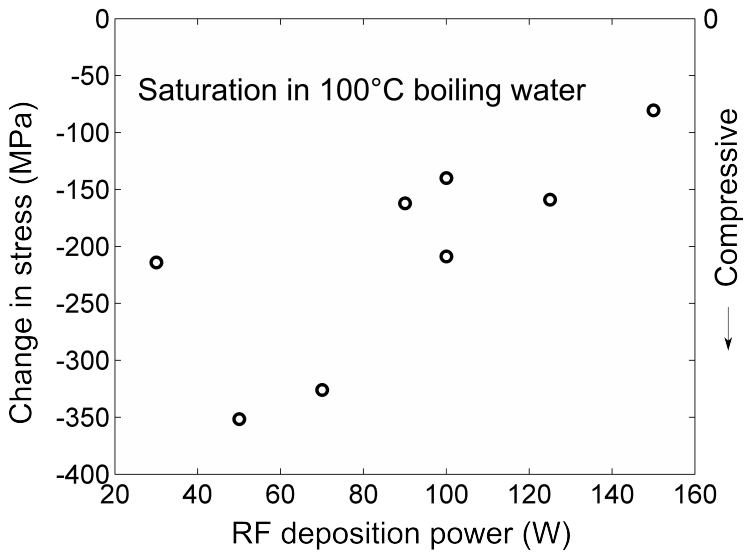

Figure 7.8: Change in mechanical stress in single-layer hybrid barrier films when exposed to boiling water, as a function of the radio frequency power used in film deposition. 'Saturation in 100 °C boiling water' means that the entire barrier film has taken up water to its solubility limit. In these experiments the films can be fully saturated because they are deposited on impermeable silicon wafers. Note that saturation would occur at times way beyond the OLED's operating life.

device. This compressive stress adds to the surface stress of the as-deposited film. The ensuing total surface stress also must stay within critical bounds.

Figure 7.8 shows by how much the saturated mechanical stress in the hybrid barrier film when exposed to boiling 100 °C water as a function of RF deposition power. Over the operating lifetime of the barrier film, the increase in stress adds to the as deposited stress. The schematic result is illustrated in figure 7.9, which plots the surface stress exerted by the hybrid barrier on the substrate during the operating life of the OLED that the film protects.

7.2 Example structures for particle encapsulation

The best way to protect the OLED is to make the top (high plasma power) layer sufficiently thick to achieve the target lifetime τ_{ML} , and to make the bezel sufficiently wide to obtain at least the same lifetime against lateral in-diffusion of humidity through the conformable middle layer. Therefore the bezel must be wide enough to ensure that the permeation time τ_{bezel} from the edge of the barrier to the OLED is equal to or longer than the permeation time from the top τ_{ML} of the barrier to the OLED. The hybrid barrier films are made from the three different layers of thickness h_{bottom},

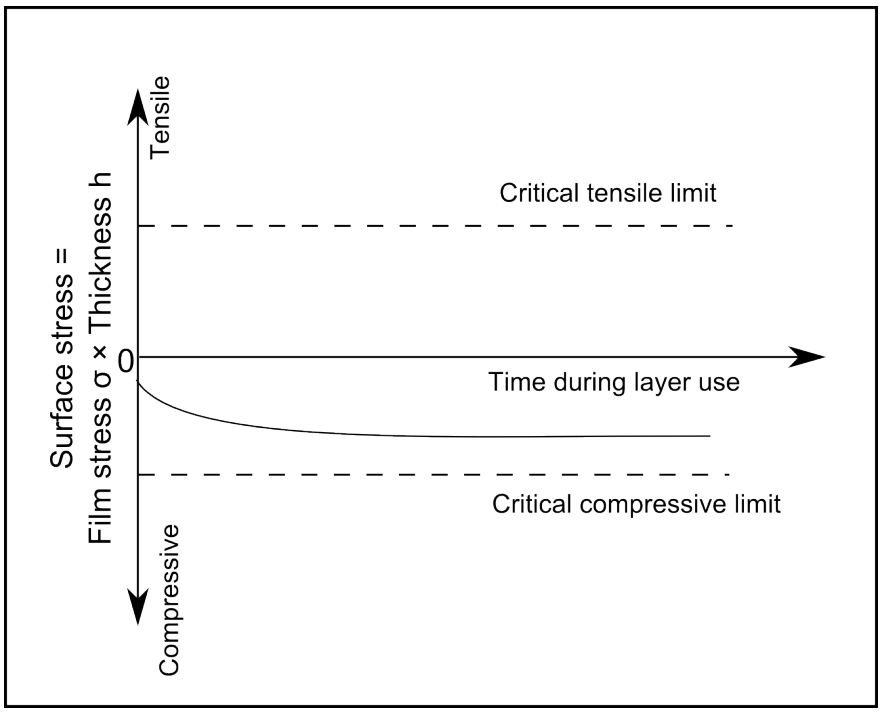

Figure 7.9: The change of surface stress in the film deposited with a compressive stress while it is exposed to humidity during use of the device that the film protects. The design goal is for the barrier film to stay within the critical limits.

h_{middle} and h_{top} and with average mechanical stress σ_1, σ_2 and σ_3 respectively. Their average stress σ_{ave} is $(\sigma_1 \times h_{bottom} + \sigma_2 \times h_{middle} + \sigma_3 \times h_{top}) \,/\, (h_{bottom} + h_{middle} + h_{top})$.

1 monolayer of H_2O will have penetrated through a 1 μm (70 W) barrier in 6 years, as shown in table 4.7. A 150 W deposited barrier has 4 times lower water diffusion coefficient than a 70 W barrier as shown in figure 7.3. To the first order, it would take 24 years for 1 monolayer to permeate a 1 μm of a barrier deposited at 150 W.

An analogous first-order calculation can be made for the lateral permeation of H_2O in the (50 W) polymer-like layer, along the width of the bezel. Its result is that the bezel must be 20 μm wide to meet the 20-year lifetime requirement. A more accurate value for the bezel width will depend on the thickness of the polymer-like layer. The bezel width may depend primarily on the rate of permeation along the *interface* between the substrate and the barrier film. This rate must be determined experimentally for each specific case.

Example 1: Barrier designed for covering 5 μm particles and $\tau_{ML} = 20$ years at 30 °C and 100% relative humidity. The three layer barrier with 1 μm bottom layer deposited at 70 W, followed by

a 2 μm middle layer deposited at 50W, and finally finished with a 1 μm top layer deposited at 150 W, will have an as deposited stress,σ_{ave} = 0 MPa (stress neutral). Due to the low diffusion coefficient of the 150 W top layer, a conservative approximation would be that the permeation is limited only by the top layer. It is assumed that as soon as the water permeates the top layer, it reaches the OLED. The stress calculations are made on the basis of this approximation. At the end of life, the top layer deposited at 150 W will have let 1 monolayer of H_2O permeate. Over the operation lifetime of the barrier, the water permeation will have changed the stress σ_{ave} from 0 MPa to -12 MPa.

Example 2: Raising the thickness of the top layer of Example 1 from 1 μm to 2 μm will make the initial stress, σ_{ave} = -20 MPa. In 64 years of operation at 30 °C and 100% relative humidity a maximum of 1 monolayer of water would have diffused through. At the end of the device lifetime, the mechanical stress, σ_{ave} will have increased to -40 MPa.

Example 3: Reducing the bottom layer thickness of Example 1 from 1 μm to 0.5 μm and the middle layer from 2 to 1.5 μm will make the initial σ_{ave} = 0 MPa. In 24 years of operation at 30 °C and 100% relative humidity, 1 monolayer of water would have diffused through the barrier film. The mechanical stress σ_{ave} will change to -17 MPa over this lifetime. Due to reduced thickness, this structure might be prone to particle induced defects. The particle size has to be reduced before employing a structure suggested by this example.

Chapter 8

Particle encapsulation in Organic Light Emitting Diodes

The projected performance of a barrier film can be confirmed only by encapsulating actual Organic Light Emitting Diodes, and demonstrating its lifetime at accelerated test conditions of high temperature and relative humidity. The diffusion measurements in chapter 4 and particle encapsulation studies in chapter 6 have enabled the design of a three layer barrier structure that can encapsulate particles (chapter 7) and has low enough permeation for water. To test this three layer barrier film design, we encapsulate bottom emitting OLEDs. Prior to barrier fabrication, the bottom emitting OLEDs are peppered with 5 μm glass beads to test the effectiveness of particle encapsulation.

This chapter describes the structure of the bottom emitting OLED, steps for adding artificial control particles and encapsulation of the OLED and discusses the results.

8.1 Bottom emitting OLED

The Bottom emitting OLEDs (BOLEDs) are fabricated by our collaborators at Universal Display Corporation. The device utilizes small-molecules for light emission and electron transport and is phosphorescent. The emitter layer comprises of UDC host and UDC green dopant. Figure 8.1 shows schematic cross section of the small-molecule OLED. The layers in the bottom emitting OLED are from bottom to top:

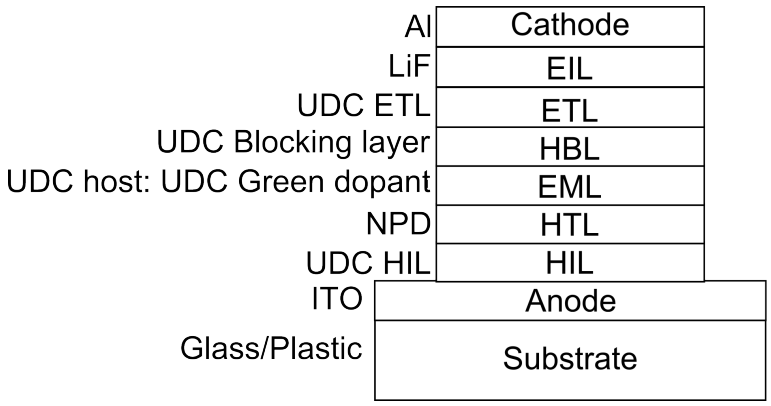

Figure 8.1: Cross section of a small-molecule Bottom Emitting OLED showing different layers. A positive voltage is applied in the anode with respect to the cathode to create a forward bias and generate light emission from the doped AlQ_3 layer. The emission from such a structure appears green in color.

1. Bottom anode layer: Indium Tin Oxide.

2. Photoresist grid (not shown in figure 8.1).

3. Hole Injection layer: UDC Hole Injection layer.

4. Hole Transport layer: NPD.

5. Emitter layer: UDC host: UDC green dopant.

6. Hole Blocking layer: UDC Blocking layer.

7. Electron Transport layer: UDC Electron Transport layer.

8. Electron Injection layer: LiF

9. Cathode: Al

The fabrication of the OLED is based on a 6×6 inch^2 mother glass. Nine identical OLED test coupons of size 2×1.5 inch^2 can be fabricated from each mother glass. The cross section and top view of an individual test coupon are illustrated by figure 8.2. The first step in OLED fabrication is the deposition on the anode layer which is either ITO or IZO. The ITO or IZO anode layer is then patterned by photolithography. A photoresist based grid is patterned by photolithography. The photoresist grid (see figure 8.1) electrically separates the pixels by making sure that current flows from the anode to the cathode only via the emissive organic layers. After the patterning of

the photoresist grid, the substrate is baked 400 °C in vacuum to get rid of any residual solvents and water dissolved in the photoresist. After the bake step, the OLED active layers are deposited by evaporation through a shadow mask. Once the final cathode layer is evaporated, the sample is taken out of the vacuum and scribed in air to separate the test coupons. After scribing the samples are loaded into a nitrogen glovebox and are sealed inside desiccant filled metal foil bags. These desiccant filled bags containing the samples are transported from the UDC glovebox to the Princeton glovebox in a span of 45 minutes. The test coupons are removed from the glove box at Princeton as and when they are required to perform encapsulation by PECVD. Figure 8.3 are top-view and bottom-view photographs of one such test coupon.

8.2 Beads on OLED

Artificial control particles spread on top of the OLED before encapsulation enable testing the particle encapsulation. If the OLEDs pass the required reliability tests, the capability of the deposition to encapsulate an OLED even in the presence of stray particles of the given size can be proven.

To study and develop the particle encapsulation nature of the proposed three layer barrier deposition, 5 μm glass beads are used. "Duke standard" silica glass beads of 5 μm diameter from Thermo Scientific are used as control particles. These beads are traditionally used as spacers in liquid crystal displays. The glass beads are indirectly sprayed on to the OLED surface using a spray chamber.

8.2.1 Surface pre-clean

Before the step of controlled addition of beads, the OLED surface is cleaned. The preceding scribing step for creating multiple test coupons from a bigger mother glass creates glass dust. Because the glass dust can go up to 20 μm in diameter it interferes with our particle encapsulation test. To get rid of the unwanted glass dust, the OLED surface is blasted with flow from a powerful nitrogen gun in a laminar flow hood under clean room conditions. The nozzle of the nitrogen gun is placed very close to the surface of the OLED to prevent any re-deposition of ambient particles that get stirred

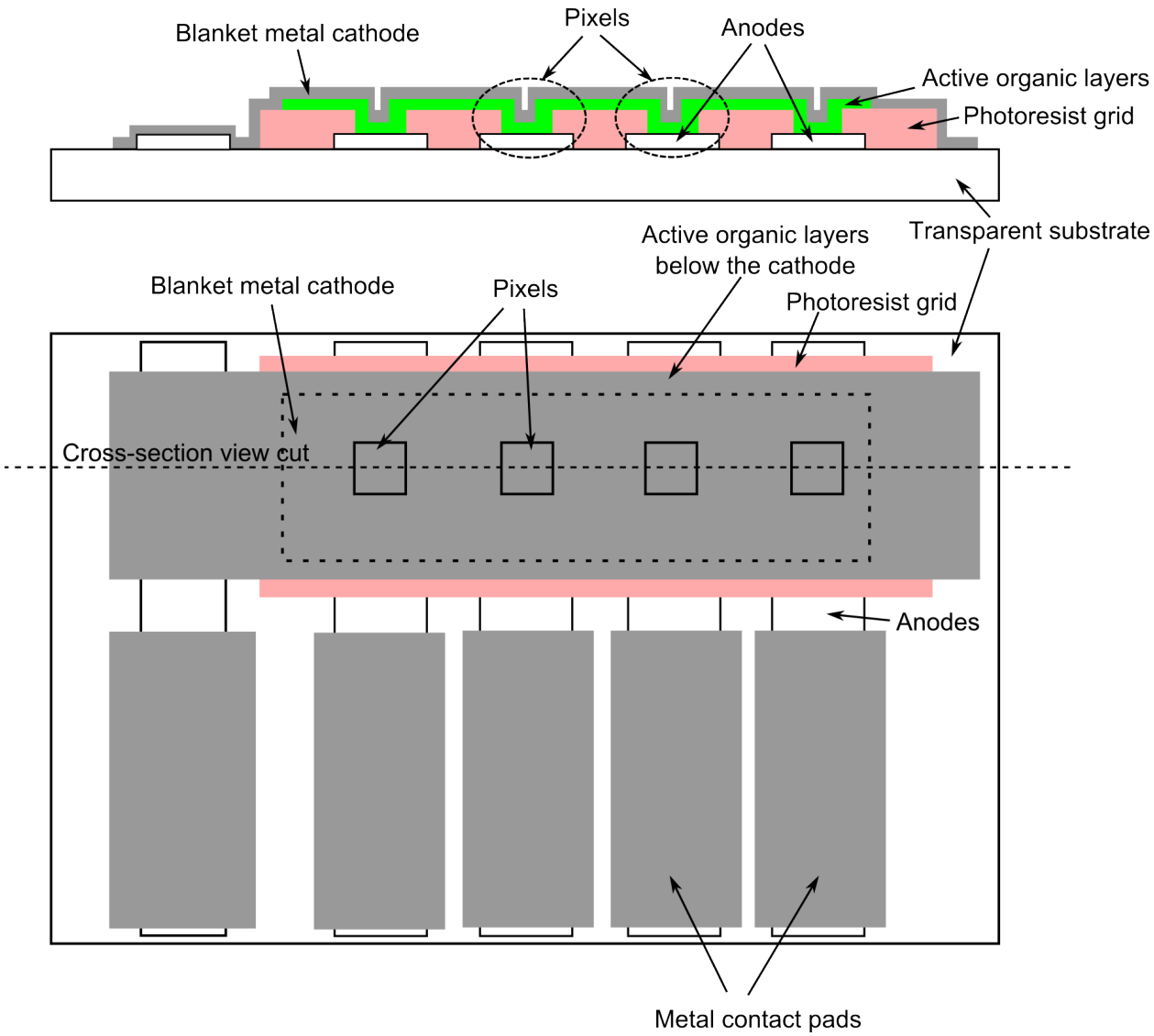

Figure 8.2: Cross section and top view of a bottom emission OLED test coupon used to study barrier encapsulation. The test coupons are 2×1.5 inches in size. Note the photoresist grid that separates the pixels from each other. There are 4 pixels per test coupon, each with an emissive area of 2 mm^2.

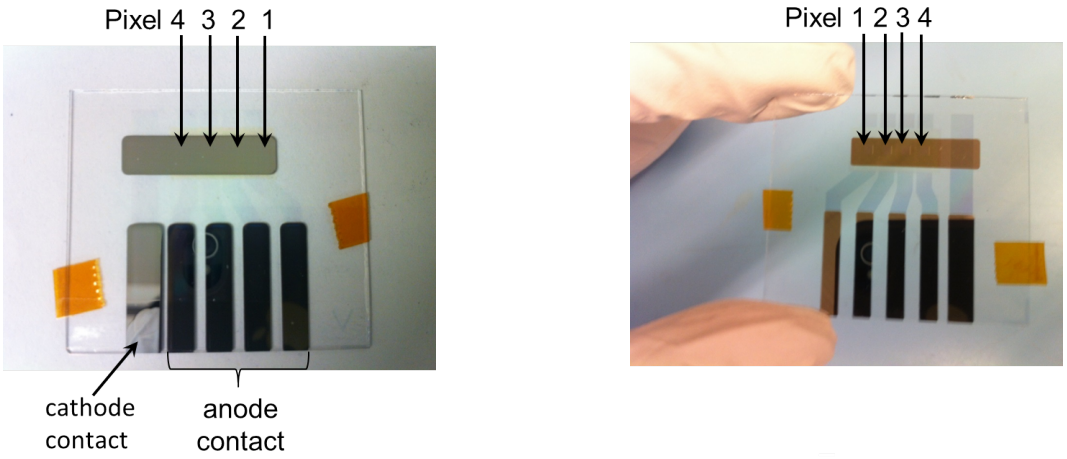

(a) Top view of the test coupon.

(b) Bottom view of the test coupon.

Figure 8.3: Bottom emission OLED test coupons used for particle encapsulation tests. Each coupon has 4 pixels. Each pixel is 2 mm^2 in area. Particles are spread on the surface of the test OLED coupons before encapsulation.

up by the nitrogen gun. This process is essential to remove the glass dust. If it is not removed, the barrier film will delaminate during accelerated testing.

8.2.2 Bead spray chamber

After the cleaning step, the glass beads are sprayed onto the surface of the OLED using a homemade spray chamber. The chamber is approximately $20cm \times 10cm \times 10cm$ in size. Figure 8.4 describes its operation. The spray chamber is a small plastic box. A 1/4 inch nitrogen inlet line is controlled by a valve and a regulator. The regulator is set at 20 psi pressure. An exhaust outlet line with a filter prevents the glass beads from leaving the chamber. A nitrogen flow cleaned OLED test coupon is placed face down inside the chamber. The test coupon is elevated by supports along the edges of the coupon so that the active area does not touch the floor of the chamber. A tweezer full of beads, approximately 50mg, is placed right at the mouth of the nitrogen line inside the chamber. The chamber lid is closed and the nitrogen valve is opened for 10 seconds. The nitrogen jet from the inlet line disperses the beads all over the chamber including the surface of the OLED. While most of the beads are individual and separate, some beads settle on the surface as clusters. The clusters are greater than $5\mu m$ in size.

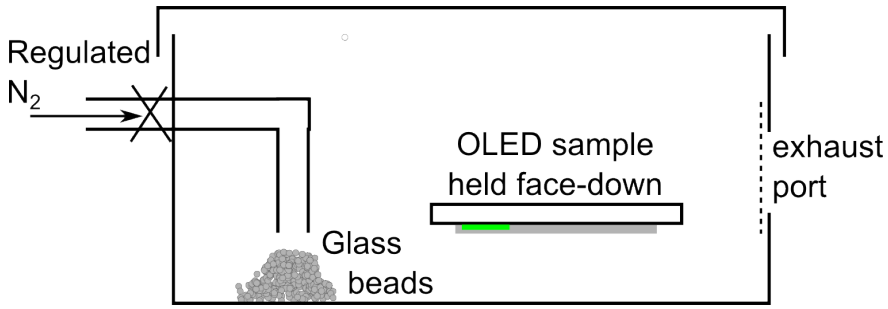

(a) A bottom emission OLED placed face-down after the cleaning step. Approximately 50 mg of 5 μm glass beads are placed right at the mouth of the nitrogen nozzle.

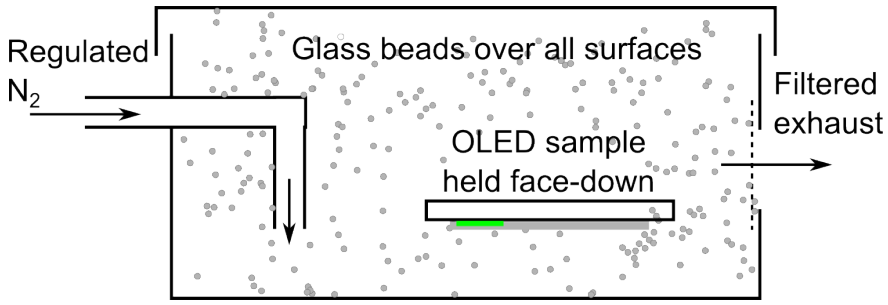

(b) Opening the nitrogen inlet coats all surfaces in the chamber with the glass beads. While most of the beads stay separate, some glass beads stick to each other forming clusters of size bigger than 5 μm.

Figure 8.4: Silica bead spray chamber with the sample positioned face-down. The nitrogen inlet is controlled by a valve. The exhaust of the chamber has a filter to prevent the escape of glass beads.

8.2.3 Surface post-clean

Figure 8.5a shows the surface of the OLED after the bead spray step. The yellow surface in the image is the aluminum cathode surface. The black spots are the spherical glass beads. While most of the beads are single there are a few cluster of glass beads on the surface. The clusters are bigger than 5 μm and affect the controlled evaluation of the OLED particle encapsulation. To remove the bead clusters a weak nitrogen jet is utilized. The weak nitrogen flow removes the heavier glass clusters from the aluminum surface and displaces some of the individual glass beads. Figure 8.5b shows the same OLED pixel after the surface post-clean. There are no glass bead clusters.

8.2.4 Glass bead adhesion

The glass beads preferentially stick to different surfaces. Figure 8.6 shows adhesion of glass beads on three surfaces: the aluminum metal cathode, the small-molecule organic emissive layers and the photoresist grid. These images were taken after an extensive post-clean step. A strong nitrogen

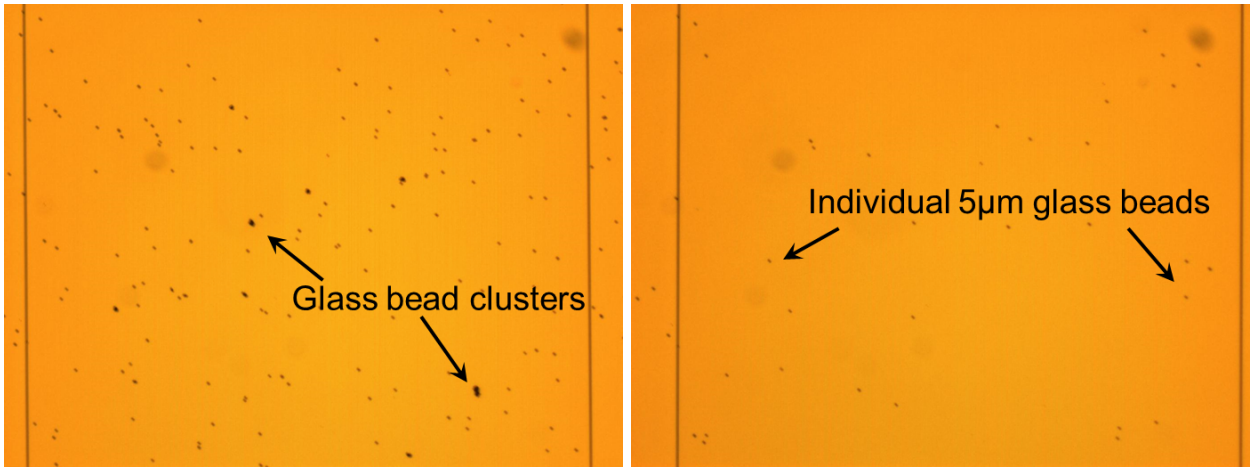

(a) An OLED pixel after the bead spray step. Single 5 μm glass beads are abundant. Few glass bead clusters are visible.

(b) The same OLED pixel after the surface post-clean step. The glass bead clusters have been removed.

Figure 8.5: Top views of a pixel with glass bead clusters and only single glass beads, before and after the surface post-clean step.

jet was used for post-clean to get rid of all glass beads. The small-molecule organic surface still showed the presence of beads. Due to the surface properties that have not yet been studied, the glass beads stick preferentially to the surface of the organic emissive layers. This results in clusters of beads resting on the surface even after the surface post-clean step. The presence of clusters would alter the controlled particle encapsulation tests. To remedy this problem for the experiment at hand, during the OLED deposition process, the aluminum cathode is increased in size to cover the entire organic emissive layer as shown in figure 8.2(where the small-molecule organic layer is hidden under the aluminum).

8.3 Encapsulation of OLEDs

Right after blowing off the glass bead clusters, the OLED test coupon is loaded into the vacuum deposition chamber for encapsulant film deposition. To reduce the impact of atmosphere on the OLED test coupons, the time between removing the sample from the glovebox to loading to the vacuum chamber is restricted to 5 minutes. Any prolonged exposure results in the oxidation of the OLED active layers which then appear as black spots in the emission image immediately after barrier deposition. After loading the OLED test coupon is pumped for 4 hours at 10^{-5}Torr pressure.

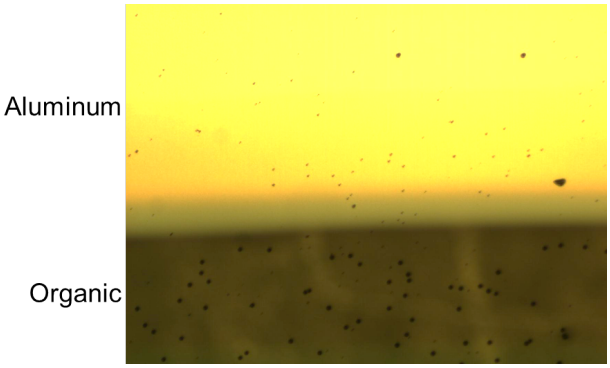

(a) Comparison of bead adhesion between an aluminum surface and small-molecule organic surface. There are 3 beads on the aluminum surface in the image and more than 50 on the small-molecule organic surface.

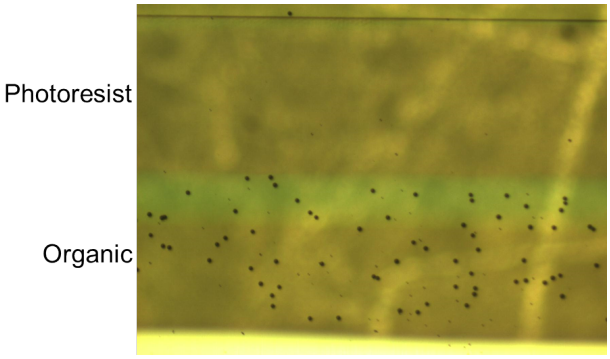

(b) Comparison of bead adhesion between a photoresist grid surface and small-molecule organic surface. There are zero beads on the photoresist surface in the image, and more than 50 on the organic surface.

Figure 8.6: Top views: comparison of bead adhesion on different surfaces after a post-clean step done with a strong nitrogen jet. The blacks dots in the image are the 5 μm beads. The image window is 2mm wide in both cases.

The deposition process starts with a nitrogen plasma treatment as given in table 8.1. Three layers are deposited in order where the bottom layer is deposited at high power, middle at low power and the top at high power again. The pressure is altered simultaneously. The flow rates of the precursors, HMDSO and oxygen are held as a constant at 1.1 sccm and 33 sccm, respectively. The total thickness of the three layer barrier film is 3.6 μm. Figure 8.7 shows a far field image of the OLED after encapsulation. The gray and black surface on the image is the aluminum metal cathode. The gray surface is part of the aluminum metal cathode that covers the small-molecule organic layer. The white dots are the individual 5 μm glass beads. Figure 8.8 shows bottom light emission from the 4 pixels in the test coupon right after deposition. The OLED coupon is flipped and the photograph of the luminescent bottom emission OLED pixels are obtained. As a result, the pixels are laterally inverted when compared to the top view image. The pixel 1 is electrically shorted with a small shunt resistance. As the lifetime test proceeded at 85 °C and 85% relative humidity, the shunt resistance increased and the pixel started lighting up (figure 8.9).

8.3.1 Environmental testing of encapsulated OLEDs.

After deposition, the sample is unloaded and subject to high temperature and humidity testing. The functioning of the environmental chamber used for the high temperature and humidity test

Table 8.1: Deposition recipe for particle encapsulation. The recipe starts with a nitrogen plasma and is followed by 3 layers. The total thickness of the barrier film is 3.6 μm.

Layer #	Precursors	Power and Pressure	Time	Thickness
-	~400 sccm nitrogen	40 W, 2 Torr	40 seconds	-
1	1.1 sccm HMDSO 33 sccm oxygen	80 W, 200 mTorr	2 hours	3.6 μm
2		40 W, 300 mTorr	1 hour	
3		80 W, 200 mTorr	1 hour	

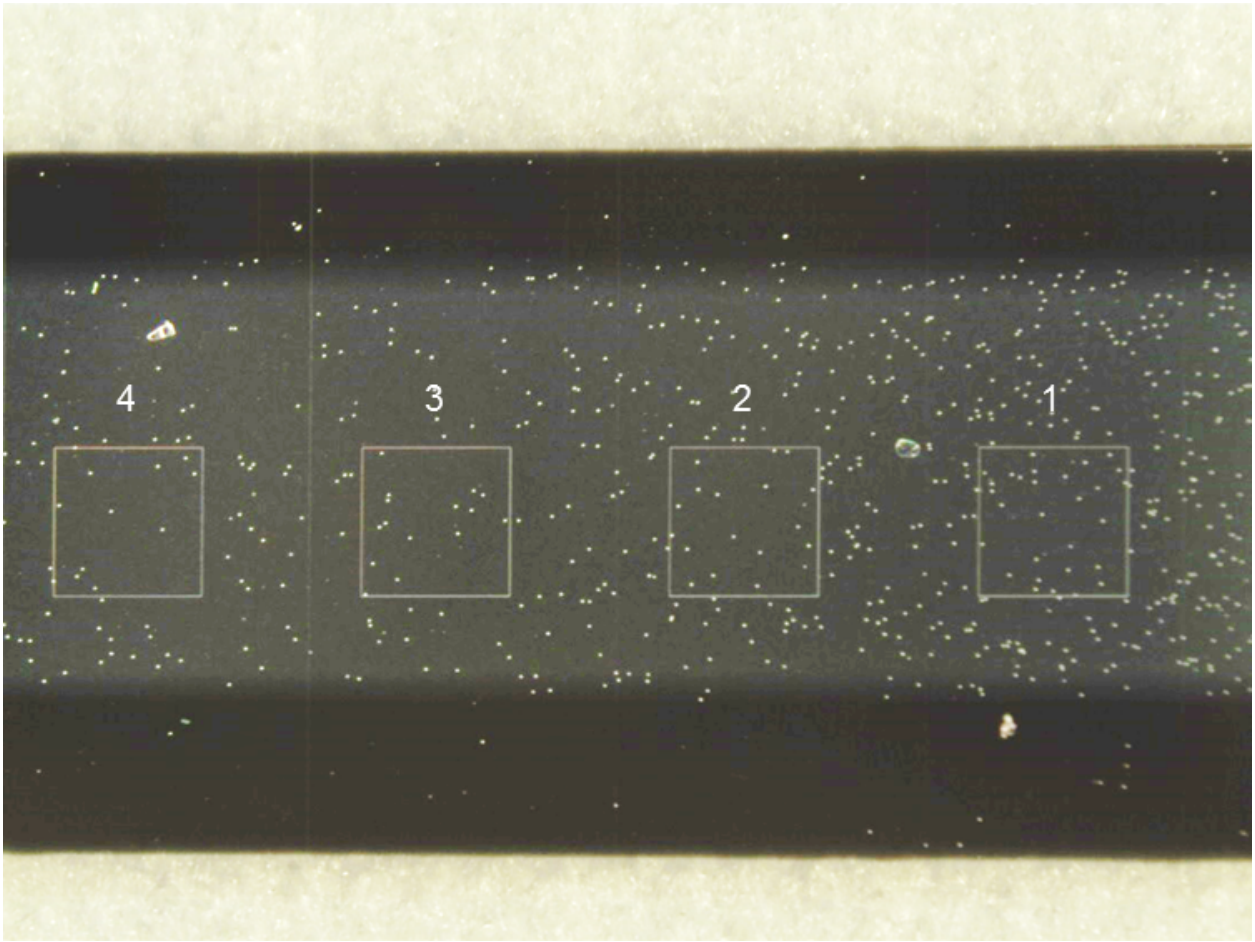

Figure 8.7: Far field top view photograph of a 4 pixel OLED test coupon with 5 μm size standard particles after encapsulation. The gray and black region together is the aluminum cathode surface. The white dots are the 5 μm glass beads. The bigger white clusters are dirt from the deposition chamber that deposited during the unloading of the OLED test coupon from the chamber. The encapsulation recipe is given in table 8.1. The pixels are numbered 4 through 1 from left to right.

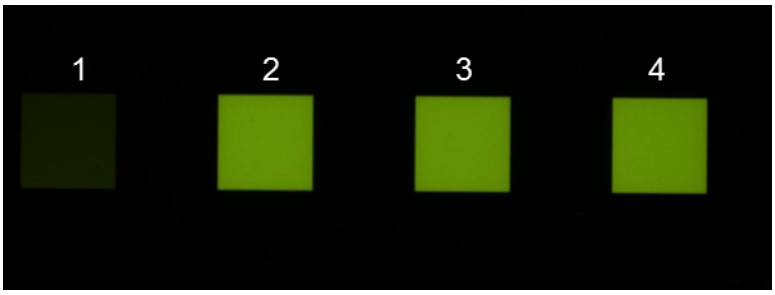

Figure 8.8: Initial image of the encapsulated bottom emitting OLED with 5 μm glass beads. The pixels are laterally inverted with respect to the top view image. The pixel 1 is dark due to high leakage current.

is described in chapter 4 and appendix A. The emission is periodically monitored by taking the sample out of the environmental test chamber and taking an image at ambient room conditions. From the images, the degradation of the OLED is evaluated. Figure 8.9 shows the bottom emission images obtained after different times under 85 °C and 85% relative humidity.

From the images it can be seen that there are no black spots that originate in the active area of the pixels. If there were breaks in the barrier film where the particles are present, the water would permeate through these breaks and oxidize the cathode and the active emissive layers. This would appear as a growing black spot on the emission image.

The top layer of the barrier film is deposited in conditions similar to the barrier layer discussed in detail in chapter 4. From table 4.7, 1 monolayer of water would permeate a 1 μm barrier layer at 400 hours at 85 °C and 85% relative humidity. The extrapolated lifetime at room temperature conditions are given. A 500 hour demonstration of particle encapsulated OLED at 85 °C and 85% relative humidity extrapolates to greater than 19 years of lifetime at 25 °C and 50% relative humidity and 6 years at 30 °C and 100% relative humidity.

Even though there are no growing black spots in the active pixel area, pixels 1 and 4 show shrinkage due to sideways permeation through the photoresist. There are defects on the barrier film far away from the active area of the pixel acting as a source for sideways permeation. Pixel 2 does not show shrinkage as it is favourably located to be far away from such defects. The following chapter deals with this sideways diffusion, and suggests ways to prevent it.

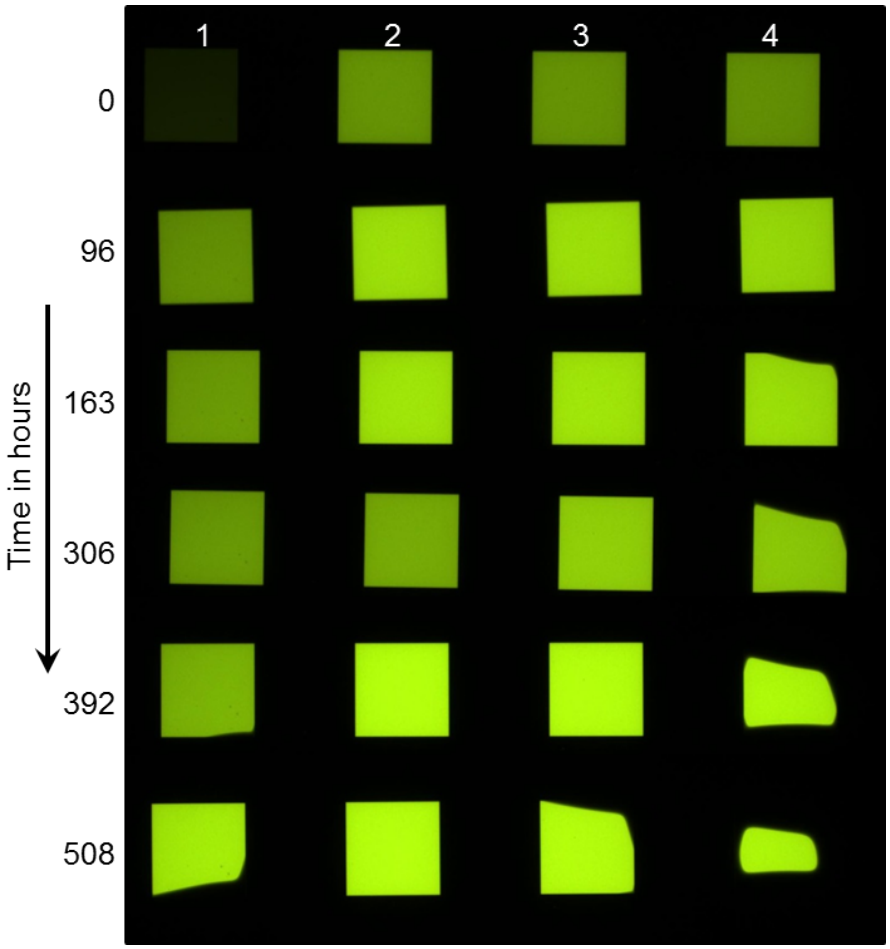

Figure 8.9: Bottom emission of the OLED pixels upon accelerated tests at 85 °C and 85% relative humidity. The OLED surface has 5 μm control glass beads acting as control particles. The three layer encapsulation is 3.6 μm in total thickness. No growing black spots are observed during accelerated testing.

8.4 Conclusion

The three layer barrier film encapsulates an OLED with 5 μm control particles without any permeation during accelerated testing over 500 hours at 85 °C and 85% relative humidity. Glass beads of 5 μm size were encapsulated with a 3.6 μm thick barrier film. All beads were successfully encapsulated, hence there is no black spot in the active area. There is shrinkage due to sideways permeation. To demonstrate a particle encapsulation for over 500 hours reaching up to 2000 hours, the sideways permeation paths need to be understood and the ensuing pixel shrinkage needs to be remedied.

Chapter 9

Yield and reliability

In the preceding chapters, a multilayer barrier film was introduced based on measurement of barrier material properties and study of particle encapsulation. A 3.6 μm three layer barrier film encapsulated an OLED containing 5 μm size glass bead particles. The OLED test coupons did not show any top down permeation at 500 hours of accelerated testing 85 °C and 85% relative humidity.

But, it may not be possible to eliminate 100% of the particles greater than 5 μm in size. The bigger particles can create defects in the encapsulation. These defects can either be on top of the luminescent pixel or the non-luminescent grid. The number and location of the defects determine:

1. Yield of the OLED device.

2. Reliability of the OLED device to function until its predicted lifetime, τ_{ML}[1].

This chapter relates the number and location of the defects to the yield of barrier film and the reliability of its predicted lifetime. In the eventuality where zero particles above 5 μm cannot be guaranteed, guidelines to achieve 100% reliability are proposed.

9.1 Observed failure in OLED test coupons

Particles bigger than 5 μm size can cause defects in the barrier film. The location of the defects determine the failure mode:

[1]The lifetime, τ_{ML}, is the time taken for 1 monolayer of water to diffuse through the barrier film to reach the OLED. The prediction of the barrier film lifetime is discussed in chapter 4.

1. Immediate failure in the form of *growing black spots* due to defects on top of the luminescent pixel.

2. Delayed failure in the form of *shrinkage* due to defects on top of the non-luminescent permeable grid.

9.1.1 Immediate failure: Defect on top of luminescent pixel

If a defect in the barrier film is present directly on top of the OLED's luminescent active area, it would result in a circular growing *black spot* that grows in size (figure 1.4a). It eventually would grow to the size of the pixel resulting in a completely black (dead) pixel. Since the defect leads directly into the OLED pixel, the black spot would appear immediately after deposition upon exposure to water vapor.

9.1.2 Delayed failure: Defect on top of permeable grid

An electrically insulating grid is required to separate individual pixels in an OLED display. In the OLED test coupons, the grid is made out of photoresist due to its ease in fabrication. Water is highly permeable in photoresist. Figure 9.1 shows how water can permeate through a defect present on top of the grid, travel sideways through the permeable grid and reach the edge of the OLED pixel area. The OLED layers above the photoresist also contribute towards sideways water permeation. The permeating water causes the OLED pixels to shrink. Due to the distance between the location of the defect on top of the grid and the edge of the OLED pixel area, the shrinkage is delayed.

Figure 8.9 in chapter 8 is a case in point illustrating the delayed shrinkage. In figure 8.9, the shrinkage in pixel 4 appears at 163 hours of accelerated testing at 85 °C and 85% relative humidity[2]. From the evolution of shrinkage in the test coupon, three defects can be identified. Their approximate locations are given in figure 9.2.

We assume that for the barrier film the average number of uncontrollable defects per sample due to particles bigger than 5 μm is three.

[2]Permeation can occur from the edge of the barrier film into the pixel active area causing shrinkage. We assume that the display/test coupon bezel is thick enough for this to not happen.

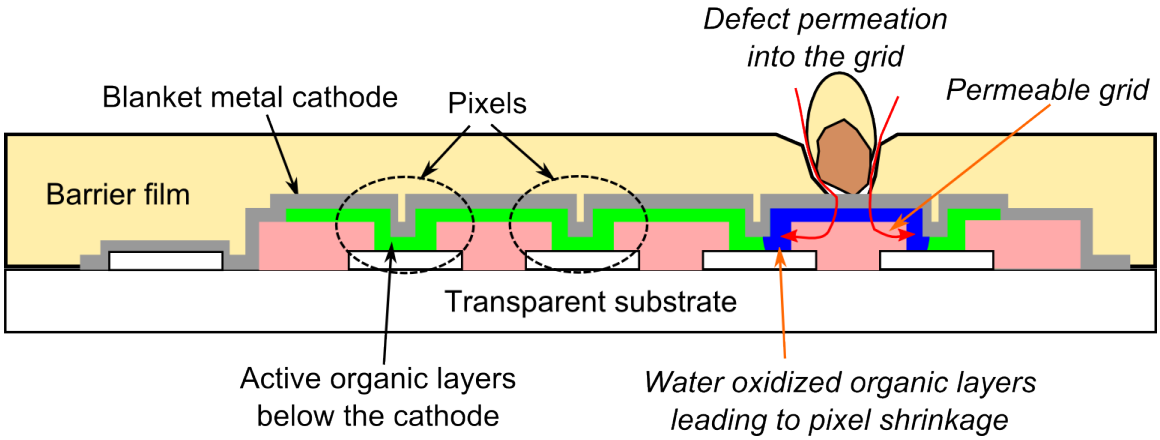

Figure 9.1: A defect in the barrier due to either particle or pin-hole can act as a conduit for water. When the defect is present on the top of a permeable grid for OLED separation, water permeates through the grid into the pixel's active area, resulting in shrinkage of the pixel.

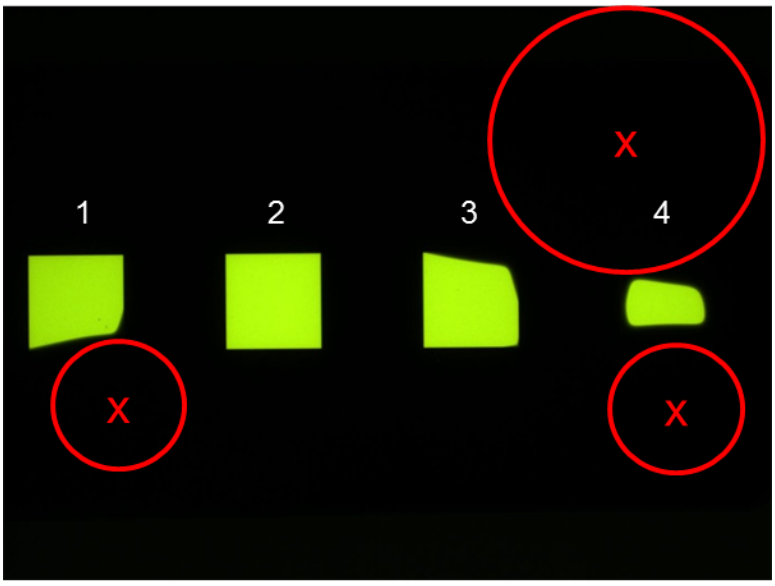

Figure 9.2: Bottom emission image taken after 508 hour testing at 85 °C and 85% relative humidity. Three defects on the barrier regions over the photoresist grid act as a conduits for water. These three defects cause pixels to shrink from their edges. The red circles qualitatively show the size of the defect. The top right defect is predicted to be bigger than the rest of the defects.

Table 9.1: Defect probabilities in the test coupons.

Area of the grid, A_{grid}	92 mm^2
Area of 1 pixel	2 mm^2
Area of 4 pixels, A_{pixels}	8 mm^2
Defect density, λ	0.03 mm^{-2}
Probability of defect in the active area	$1 - e^{-\lambda \times 8 \text{ mm}^2} = 21.3\%$
Probability of defect in the grid area	$1 - e^{-\lambda \times 92 \text{ mm}^2} = 95.1\%$

9.2 Defect location prediction

The number of barrier defects that cause growing black spots and shrinkage in the device is a random variable that follows a probabilistic Poisson distribution. For a defect density, λ, total area of the pixels, A_{pixels}, and grid area, A_{grid}, the probability to have one or more defects in the pixel area and the probability to have one or more defects on top of the grid is given below.

$$\text{Probability to have one or more defects in the pixel area} = 1 - e^{-\lambda \times A_{pixels}} \tag{9.1}$$

$$\text{Probability to have one or more defects on top of the grid} = 1 - e^{-\lambda \times A_{grid}} \tag{9.2}$$

The ratio of luminescent area in pixel to the total area allotted to the pixel is defined as *Aspect Ratio*[3]. In the test coupons, the area of the photoresist 92 mm^2 is much bigger than the total area of the active pixels, 8 mm^2 as shown in figure 8.1 resulting in an aspect ratio of 8%. Due to the difference in area between the pixels and the grid, in these test coupons, the defects have a high probability of lying on top of the grid.

Since on an average there are three defects per OLED test coupon, the defect density, λ, is 0.03 mm^{-2}. From the Poisson distribution, the probability to have one or more defects on top of the grid of area 92 mm^2 is 95.1%, and the probability to have a defect on top of the luminescent area of 8 mm^2 is 21.3% (table 9.1).

This suggests that 21.3% of the samples would show immediate growing *black spots* in the active area and 95.1% of the samples would show delayed *shrinkage*. Only $0.787 \times 0.049 = 3.9\%$ of the devices would have neither growing black spots nor show shrinkage and would show degradation purely by bulk diffusion.

[3]In displays, the aspect ratio is around 20-30% due to shadow mask alignment limitations.

9.3 Yield and reliability

For (1) speeding up research and (2) achieving commercial viability, high yield and reliability for an OLED device are required. In the OLED test coupons, 21.3% of the devices would have in-pixel defects that show up as growing black spots immediately and 95.1% of the samples would show delayed shrinkage. These two numbers determine the yield and reliability of lifetime prediction in the OLED test coupons.

9.3.1 Yield

Under the situation where the defect density in an OLED device is λ, a fraction equal to $\left(1 - e^{-\lambda \times A_{pixels}}\right)$ of the OLED devices would show immediate growing black spots. All devices can be screened after deposition and the devices that show growing black spots can be discarded. An example screening step could be a 10 hour accelerated test at 85 °C and 85% relative humidity after fabrication and before the devices are put to use. After screening, the yield is:

$$\text{Yield} = e^{-\lambda \times A_{pixels}} \tag{9.3}$$

The yield drops exponentially with the area of the display, $A_{display}$ for a fixed aspect ratio.

$$\text{Yield} = e^{-\lambda \times A_{display} \times \text{Aspect ratio}} \tag{9.4}$$

Reducing the size of the display, $A_{display}$ increases yield. For a given display size, the yield can be improved by reducing the defect density, λ, or by reducing the aspect ratio.

In the OLED test coupons, there are three defects per sample on an average. The estimated yield hence is 78.7%.

9.3.2 Reliability

Among the samples that have passed the yield screening step and are put to use, $\left(1 - e^{-\lambda \times A_{grid}}\right)$ of the devices would have one or more defects on top of the grid. If the grid is permeable, these defects would result in OLED pixel shrinkage before the end of the lifetime predicted by permeation

measurements given in chapter 4. The reliability that a pixel will not show shrinkage before the lifetime predicted by permeation measurements is:

$$\text{Reliability of the predicted lifetime} = e^{-\lambda \times A_{grid}} \tag{9.5}$$

In the OLED test coupons, the reliability of predicted lifetime is a low 4.9%. This low reliability has disadvantages:

1. *In commercial displays*, a low reliability for the predicted lifetime of 4.9% is not viable. In electronic gadgets, over 99% reliability for the display may be required as a failed display equates to a failed gadget.

2. *In particle encapsulation studies of OLED test coupons*, the shrinkage and hence low reliability causes the pixels to go black before the effects of top-down permeation can be evaluated. In this research project, over 100 samples were fabricated. All samples suffered from shrinkage. Removing shrinkage is necessary to increase the barrier film operational lifetime in BOLED devices.

9.3.3 Guidelines of achieving 100% reliability

To achieve 100% reliability of predicted lifetime, shrinkage needs to be prevented. A barrier film is designed for encapsulating particles smaller than *critical size*. In chapter 8, the a 3.6 μm film was designed to encapsulate 5 μm size particles. Shrinkage is caused by defects that have been introduced by particles bigger than the critical size. The straightforward way to prevent shrinkage is to eliminate all particles above the critical size resting on top of the grid that than can cause a defect in the barrier film. But so far this has been extremely challenging. The other way to obtain high reliability is by achieving zero sideways permeation. If the path for water to permeate from the defect on top of the permeable grid into the OLED active area is blocked, the shrinkage can be eliminated. The path comprises of the permeable grid and the organic layers.

It should be emphasized that all devices need to be subject to a screening test[4] right after fabrication to pick up in-pixel defects. In the screening process, the samples with in-pixel defects are discarded and yield is calculated.

[4] An example screening test would be 10 hours at 85 °C and 85% relative humidity.

9.4 Conclusion

The number and location of defects in the barrier film determine the yield and reliability of the predicted lifetime. Sideways permeation reduces the reliability in encapsulated OLED devices. It results in shrinkage of the pixels. Photoresist and OLED layers are responsible for the sideways permeation. To achieve 100% reliability all sideways permeation from top of the grid to the bottom active pixel area have to be eliminated.

Chapter 10

Inorganic Grid

The delayed failure in the form of shrinkage described in the preceding chapter has two major disadvantages: 1. It reduces the reliability of predicted lifetime given by permeation measurements. The reliability of the predicted lifetime in the encapsulated OLED test coupon is 4.9%; 2. It prevents research progress as the shrinkage causes the pixel to go completely dark (dead pixel) before the limits of top-down permeation can be evaluated. The OLED test coupon described in chapter 8 is a case in point. We are unable to test the particle encapsulation for over 500 hours because the pixels started to shrink. The conduits for water that cause shrinkage are:

1. Defects on top of the permeable photoresist grid.
2. Permeable photoresist grid.
3. Permeable organic layers between the grid and the metal cathode.

To improve reliability and to extend the accelerated testing period in the test coupons, the permeation paths need to be blocked. In the case where particles that cause the defects cannot be eliminated, which is the situation we face in our research lab, the sideways permeation needs to be removed. In this chapter, we propose the use of an inorganic grid to eliminate the shrinkage.

10.1 Photoresist permeability

The combination of permeable photoresist and permeable organic emissive layers form the sideways permeation path. The permeation rates in these two layers are different. At $t = 508$ hours, pixel 4 in figure 8.9 has uniform shrinkage. For this to happen, the water permeation rate in the photoresist must be much higher than the permeation rate in the organic layers. Water surrounds a pixel along the photoresist edge boundaries faster than it is able to permeate into the pixel through the organic layers. As a result pixel 4 shrinks uniformly from all edges.

10.2 Removing pixel shrinkage: Inorganic grid with overhang

To eliminate the sideways permeation and hence shrinkage, we propose using an inorganic grid to replace the highly permeable photoresist grid. This restricts the sideways permeation pathway to the less permeable organic layers of the OLED. The inorganic grid is made from the barrier material. Figure 10.1 illustrates this grid.

To prevent the water permeation in the organic layers of the OLED, an *overhang* structure is proposed. The overhang structure creates a discontinuity in the permeable organic layer. Water permeating sideways on the organic layer is stopped at the edge of the pixel area (see figure 10.1).

10.2.1 Experimental procedure

To come up with an overhanging inorganic grid, different recipes were tried out on a silicon wafer substrate and the cross sections were viewed in the SEM. Figure 10.2 shows the SEM cross section of the inorganic grid made from the final recipe given below.

1. *Lift-off resist pattern:*
    1.1. 5 minute prebake at 95 °C
    1.2. 40 second, 4000 RPM, HMDS spin,
    1.3. 40 second, 4000 RPM, LOR3A spin,
    1.4. 3 minute 150 °C bake,
    1.5. 40 second, 4000 RPM, AZ5214 spin,
    1.6. 1 minute, 95 °C softbake,

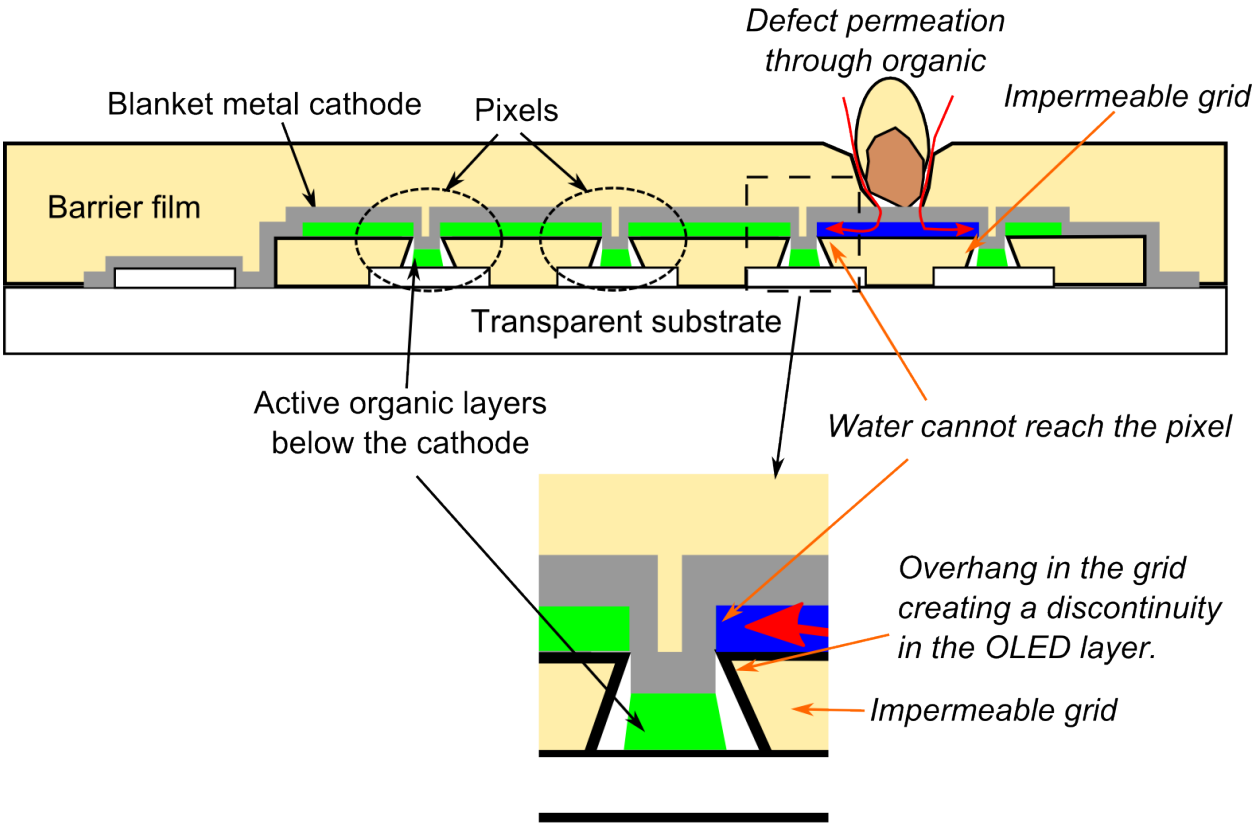

Figure 10.1: Schematic of an impermeable, inorganic grid that prevents the sideways permeation seen in photoresist. An overhang in the grid creates a discontinuity in the organic emissive layer. The aim of the organic emissive layer discontinuity is to prevent the sideways diffusion through the organic layer. The oxidized organic layers are shown in blue. Permeation of water in the organic layer is stopped at the overhang.

1.7. 45 second UV exposure in MA6 mask aligner.

1.8. 2 minute development in AZ300MIF.

2. *Deposition of barrier film:* 14 min hybrid deposition: 80 W, 200 mTorr, HMDSO 1.1 sccm, oxygen 33 sccm.

3. Overnight liftoff the barrier film at 50 °C, solvent: 1165.

10.2.2 BOLEDs with grid of hybrid material, 5 μm bead particles and 3-layer hybrid barrier

The inorganic grid with an overhang is incorporated in the OLED test coupon fabrication process. The barrier film based grid is fabricated after patterning the ITO anode and before evaporating

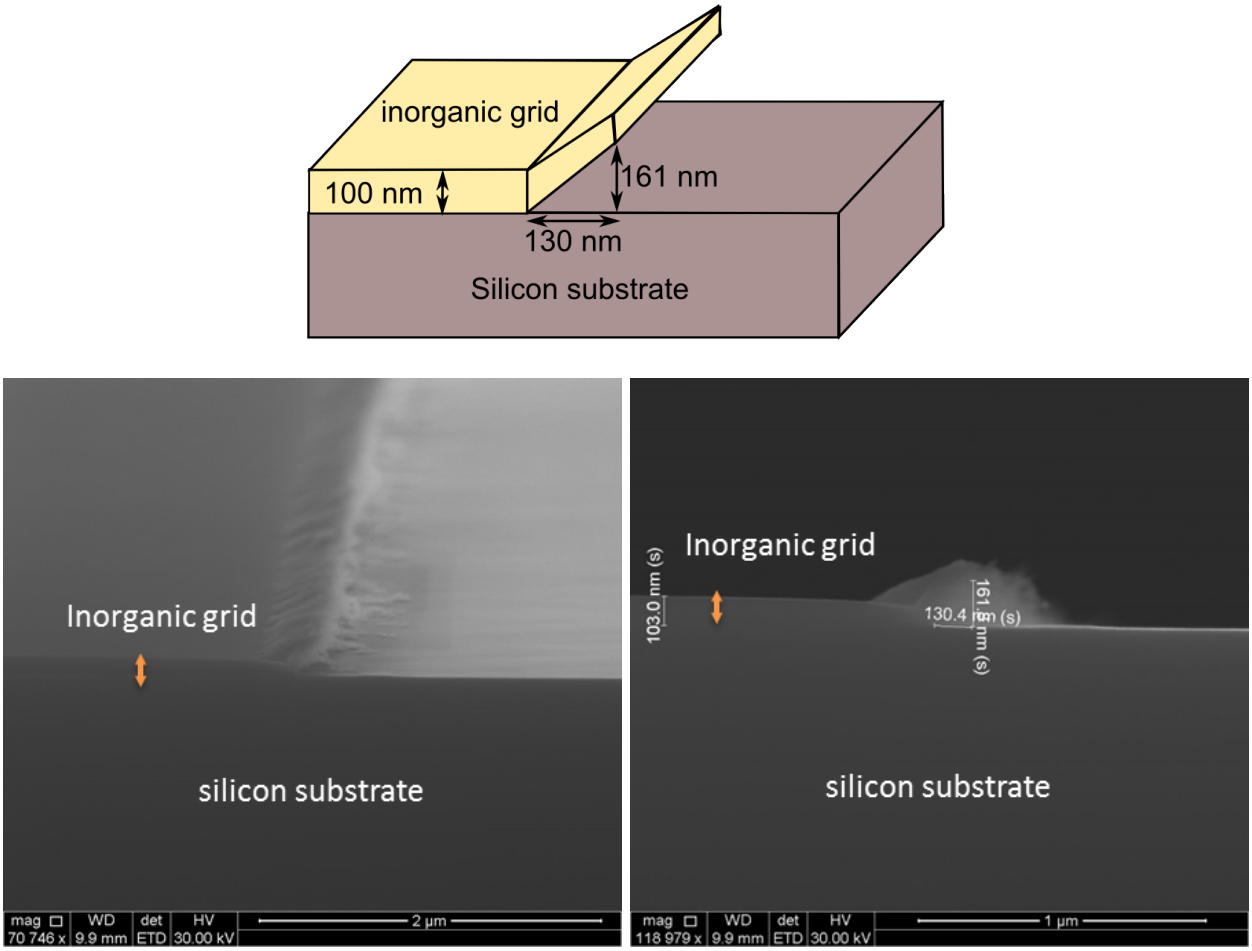

Figure 10.2: Schematic and SEM images of a 100 nm thick inorganic grid on a silicon wafer substrate. In the images, the grid is on the left. The right side of images have the exposed silicon substrate. An overhang is observed at the edge of the grid. The overhang edge is 161 nm tall and protrudes a distance of 130 nm horizontally.

Table 10.1: Deposition recipe for the barrier film on an OLED test coupon with an inorganic grid and 5 μm size glass bead particles. The recipe starts with a nitrogen plasma and is followed by three deposition layers.

Layer #	Precursors	Power and Pressure	Time	Thickness
-	Nitrogen	40 W, 2 Torr	40 seconds	-
1	1.1 sccm HMDSO 33 sccm oxygen	80 W, 200 mTorr	2 hours	3.9 μm
2		40 W, 300 mTorr	1 hour	
3		80 W, 200 mTorr	1 hour	

the OLED active layers. After the evaporation, 5 μm glass beads are spread and the three layer barrier is deposited with steps given in table 10.1. The resultant sample has a lot of beads. The sample is subject to 85 °C and 85% relative humidity accelerated testing for 213 hours.

10.2.3 Results

Figure 10.3 shows the degradation of bottom emitting pixels at 85 °C and 85% relative humidity accelerated testing for 213 hours. Out of the 4 pixels, pixels 1 and 2 were shorted due to imperfections in the fabrication of the grid. Pixel 3 shows no degradation at 213 hours. Pixel 4 is affected by two defects. The one on the active area causes a growing black spot. The other on the grid causes shrinkage from the bottom edge.

10.2.4 Discussion

The aim of the inorganic grid was to completely eliminate shrinkage. The bottom of the pixel 4 shows shrinkage starting at 64 hours at 85° and 85% relative humidity as shown in 10.3. We have failed to eliminate the shrinkage.

Figure 10.4 compares the shrinkage profiles between OLED test coupons containing a photoresist grid and a hybrid barrier grid. The photoresist grid shows uniform diffusion along the pixel edges, while in the inorganic grid, the edges of the pixel are sharp and well defined. The exact position of the defect can be identified by completing the circular defect as show in figure 10.4b. This suggests only one layer is responsible for the sideways permeation and it is the organic layer. The permeation through the grid has been eliminated.

The *overhang* design to create a discontinuity (figure 10.1) to stop the permeation at the edge of the pixel active area has not been successful. The organic layer still shows shrinkage/sideways

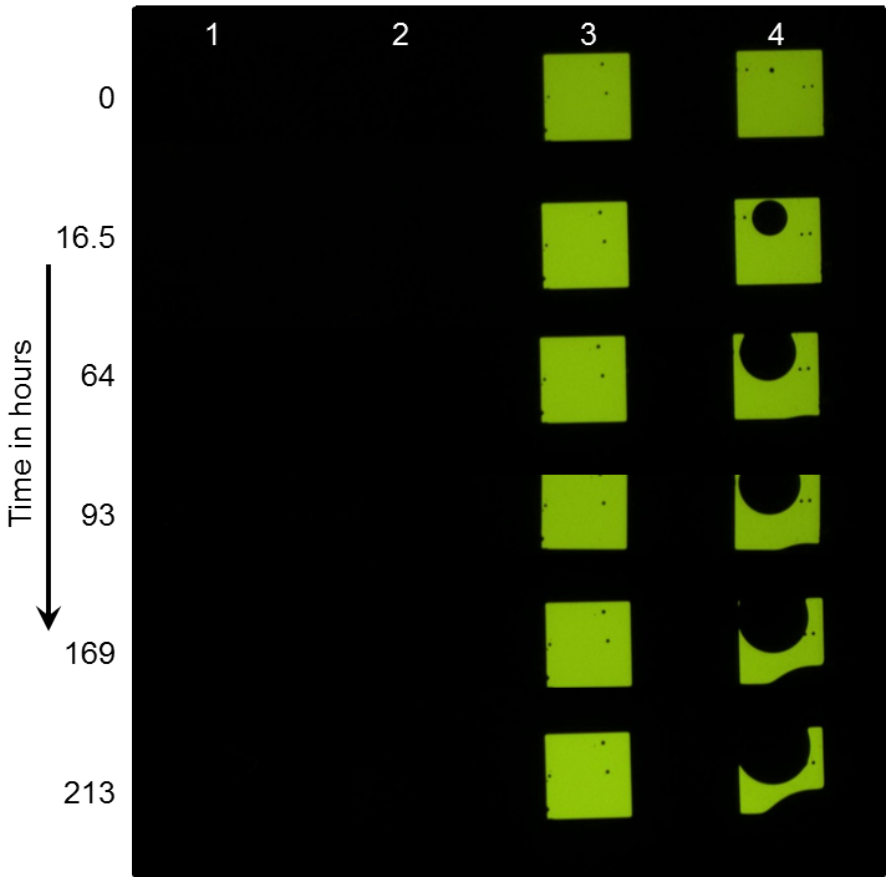

Figure 10.3: Bottom emission of the OLED pixels after different test times at 85 °C and 85 % relative humidity. The grid is made of hybrid barrier material. Pixels 1 and 2 were not powered as the cathode and the anode were electrically shorted due to irregularities in the inorganic grid.

permeation (figure 10.3). New grid designs and evaporation techniques need to be evaluated to stop the organic layer sideways permeation into the pixel area and hence obtain high reliability of predicted lifetime. We propose this as future work for the reader.

Discussion: rate of black spot growth

Pixel 4 has a growing black spot in the active area. Figure 10.5 plots the square of the area of the growing black spot as a function of time. The square of the area is linear with time. If the water uptake is assumed to be proportional to the area of the defect, then the square of the water uptake is linear with time. The same relationship was observed in thin film barrier sheets (equation 4.9). If most of the diffusing water does not react with the organic layers, then the water uptake would be faster than a thin film in a plane. This is due to the dilution introduced by structural change

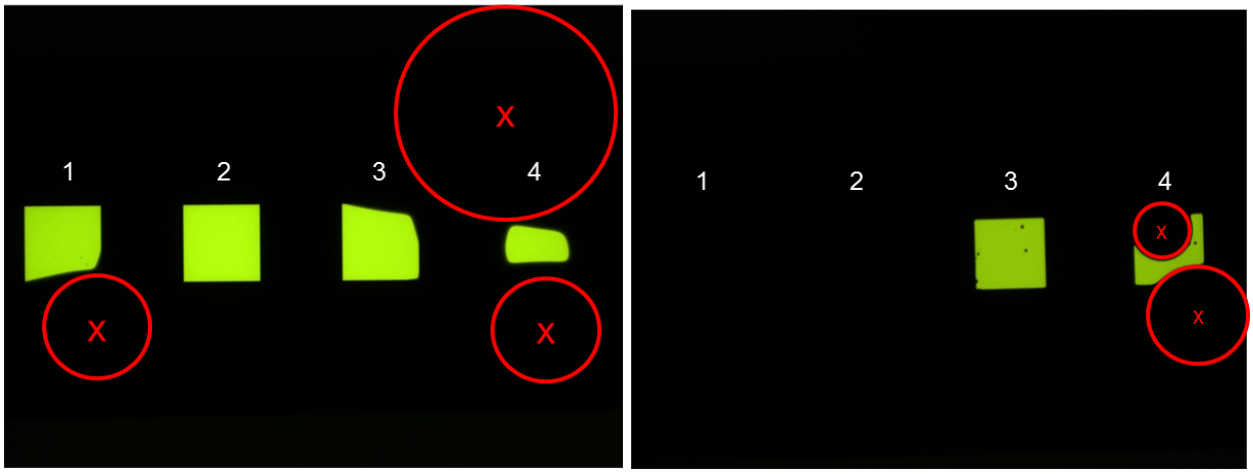

(a) The photoresist grid results in uniform shrinkage of pixel 4. The defect location responsible for shrinkage is approximately identified.

(b) The defect and shrinkage shows sharp segments. The defects centers are accurately determined by completing the circle.

Figure 10.4: Comparison of water permeation between photoresist grid and inorganic grid.

from moving from a plane sheet to a cylindrical structure. The slower growth of black spot with time and hence the slower uptake of water suggests that not only the transport of water to the dark/luminescent boundary but also the rate of the chemical reaction that occurs at the boundary determines the rate of black spot growth.

The rate limiting step for permeation can be used to understand the growth of the black spot. Two easily understandable modes of permeation and their relationship with time are:

1. If the water flux through the defect is the rate limiting step, the black spot area would grow linearly with time.

2. If the reaction of water at the edge of the black spot is the rate limiting step and the black spot is saturated with water, then the black spot area growth would be linear with the square of time.

In our samples we observe that the increase in area of the black spot is linear with the square root of time. The growth of the black spot slows down over time. Explaining this demands more involved study. We stop the discussion of the growth of black spot at this point.

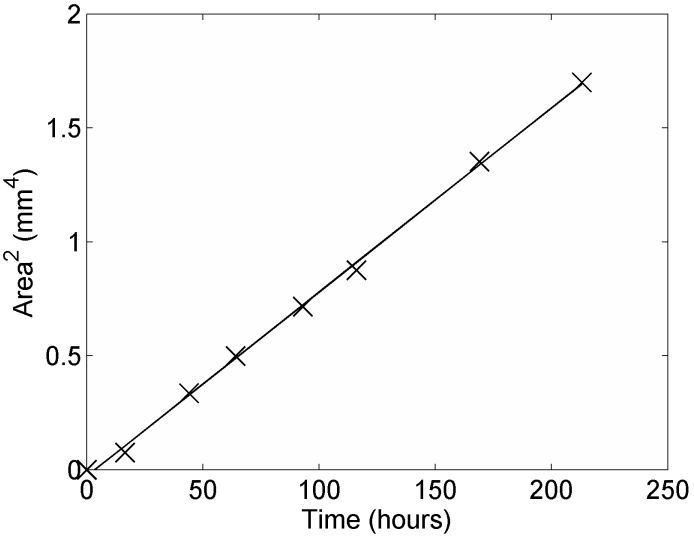

Figure 10.5: Black spot area in pixel 4 of the OLED coupon.

10.3 Conclusion

Photoresist and organic layers are responsible for the sideways permeation of water with the photoresist permeation being the dominating mode. An impermeable inorganic grid prevents the sideways permeation through the photoresist. Designing a new grid and tuning organic evaporation is necessary to prevent water from reaching the pixel via the organic layers. Achieving zero shrinkage by preventing all sideways permeation would give 100% reliability of the lifetime predicted by permeation measurements.

Chapter 11

Conclusion

Barrier films are required to encapsulate flexible Organic Light Emitting Diodes. Water permeates through 4 modes in the barrier film, namely, through microcracks, through the bulk of the barrier film by diffusion, through particle induced cracks and sideways through permeable grid layer. The development of a reliable barrier film has been difficult owing to multiple modes of failure acting simultaneously. We have managed to separate these failure modes and have addressed them one at a time.

Quantitative techniques for evaluating the diffusion coefficient and solubility of barrier materials by measuring electrical capacitance and mechanical have been described. The techniques are calibrated against secondary ion mass spectrometry for obtaining solubility. These techniques are novel as they circumvent the effect of particles and defects, which the existing techniques are incapable of doing. A set of PECVD based silicon dioxide-silicone hybrid barrier material is characterized with these robust techniques.

Particle contamination on the surface of an OLED is another bottleneck in barrier film development that has been addressed. Systematic study of particle encapsulation with fixed sizes of artificial particles was performed, and a three layer barrier film made of the hybrid material was designed. This three layer barrier film provides necessary permeation protection, encapsulates 5 μm particles and has mechanical stress within bounds to prevent delamination. As a demonstration of performance of the barrier film against particle contamination, an OLED test coupon lasted 500

hours at 85 °C and 85% relative humidity even though 5 μm size glass beads had been spread over the surface of the OLED prior to the barrier film deposition.

In the eventuality where all particle induced defects cannot be eliminated, sideways permeation of water through the permeable grid and organic layer below the barrier film reduces the reliability of the lifetime predicted by permeation tests. A defect on top of the luminescent pixel area results in a drop in yield and a defect on top of the permeable grid causes a drop in reliability. An inorganic grid is introduced to prevent sideways permeation through the permeable grid.

We have shown a systematic approach to address all forms of failure due to water permeation that is observed in an OLED encapsulated with a thin film barrier. Emulating these steps, the research and development of barrier films can be sped up. Using these steps, we have demonstrated a reliable hybrid barrier film that can provide necessary protection to provide an OLED lifetime of over 10 years.

11.1 Future Work

This thesis addressed three mechanisms that prevent the successful encapsulation of OLEDs. A lot more work needs to be done to obtain flexible, reliable OLED based products that can be used in day to day life. Some of which are:

11.1.1 Improving OLED reliability

As described in chapters 9 and 10, sideways permeation dramatically reduces the reliability of lifetime prediction by causing shrinkage of OLED pixels. A means to remove sideways permeation is necessary to obtain reliable OLEDs. Sideways permeation can be eliminated by introducing an inorganic grid for pixel separation and simultaneously controlling the geometry in which emissive organic layers and cathode are deposited. Achieving this would further the pace of moving to the thin barrier films that industry needs for flexible displays.

11.1.2 Flexible encapsulation

This thesis has studied barrier films that can be used on plastic substrates but has not demonstrated barriers on plastic. The demonstrated OLEDs all were made on glass substrates. To move to flexible substrates we need to:

1. *Characterize the critical strain in the barrier film*: For a given thickness of substrate and given neutral plane engineering, this strain has to be within compressive and tensile bounds to prevent cracking of the film or its delamination. Both the as-deposited intrinsic stress and the stress change due to water uptake need to be factored in.

2. *Design a barrier film on a plastic substrate that would be interposed between the substrate and OLED*: Water will permeate through the substrate to reach the OLED. The direction of permeation is same as that of barrier film growth. This will necessitate a new design for a three layer barrier film that encapsulates particles on the substrate.

11.1.3 Independent control of water permeability and mechanical stress

Currently the permeability of the film can be controlled by changing the radio frequency deposition power in the PECVD. But doing so changes the mechanical stress of the film. A multilayer films is hence employed to compensate for this mechanical stress. If a way to tune the water permeability of the barrier materials without altering the mechanical stress by changing the deposition conditions could be identified, a more simpler, thinner barrier film can be designed.

In this work, only the space of power and pressure tuning during deposition have been explored. More parameters such as input gases, flow rates, PECVD design can be explored to achieve this independent tuning.

Appendix A

Environmental test chamber

A.1 Introduction

High temperature and humidity are required to accelerate the permeation of water. The relative humidity of moist air is defined as the ratio of partial pressure of water to the saturation water vapor pressure at a given temperature. The water vapor pressure and density determines the quantity of water present at given temperature.

$$\text{Relative Humidity RH (in \%)} = \frac{\text{Partial pressure of water, } P_w}{\text{Saturation water vapor pressure, } P_s} \times 100 \tag{A.1}$$

The standard pressure for accelerated test is 1 atmosphere. As a result pure steam at 100 °C has 100% relative humidity.

To obtain the activation energy of the solubility and of the diffusion coefficient of water in barrier materials (chapter 7), a test apparatus that can operate at a wide range of temperature and water vapor pressure was built. The same equipment was used for the accelerated degradation tests for OLEDs at 85 °C and 85% relative humidity of chapters 8 and 10. A list of symbols is given in table A.1. Figure A.1 shows photographs of the chamber and its controls. The setup consists of three parts:

1. Heated steam source (bubbler/boiler).

2. Heated conduit for steam.

Table A.1: Symbols and units

	Symbol	Units
Temperature	T	°C
Relative humidity	RH	%
Saturated Water Vapor Pressure	P_s	atm
Partial Pressure of Water	P_w	atm
Dew Point	T_d	°C

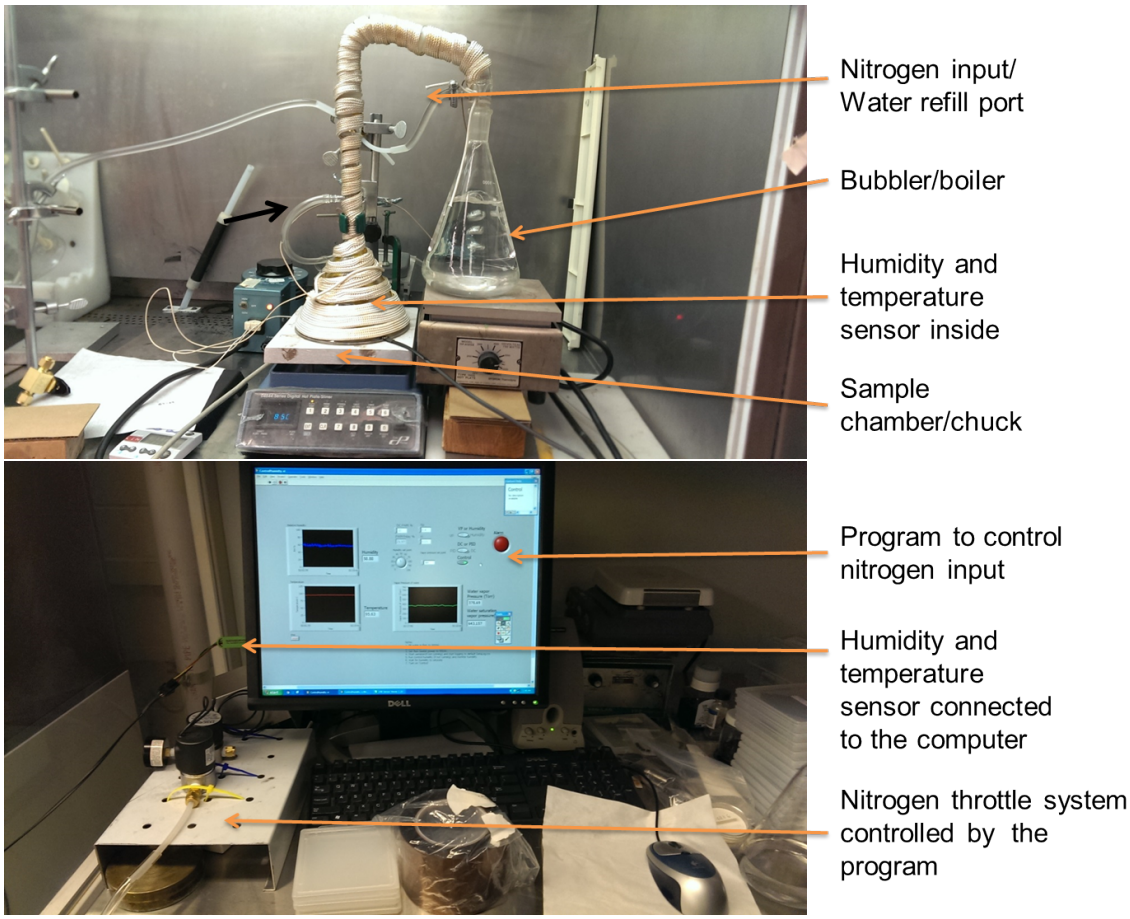

Figure A.1: High temperature and relative humidity environmental testing setup that can be controlled from 40 °C to 200 °C and 0.03 to 1 atmosphere water vapor pressure.

3. Chamber, which is an inverted glass funnel positioned on a temperature controlled hot plate.

A.2 Operation

A.2.1 Temperatures below 100 °C

The water vapor from the steam source flows through the heated into the chamber. There the water vapor leaks out of the chamber into ambient air. For T below 100 °C, the water source functions as a bubbler with nitrogen as the carrier gas. The nitrogen input is throttled to maintain a specific partial pressure of water P_w inside the chamber. The temperature of the water source is set 2 °C above the dew point T_d. The water vapor heating column is set at the test temperature, T. The sample chuck is also set at the operation temperature T. The sample is placed on the chuck. A temperature and relative humidity probe is held just above the sample. From the temperature and relative humidity, the vapor pressure of water is calculated. The vapor pressure is used as a feedback for controlling the nitrogen input throttle. The system operates in closed loop and maintains the temperature and humidity for several months only to pause once a week to fill up the water in the source.

For the electrical capacitance and mechanical stress measurements done below 100 °C, the samples were dunked in a bath of water at the test temperature T. The bath of the water consists a glass beaker containing water on a temperature controlled hot plate. The hot plate measures the temperature of the water bath through a resistor temperature detector (RTD) and uses it a feedback to set the temperature of the hot plate surface. By this the water bath temperature is held constant within an error of ±1 °. The beaker is closed with a lid. A reflux condenser connected to the lid traps escaping water vapor and returns it to the water bath.

A.2.2 Temperatures above 100 °C

For temperatures above 100 °C, the vapor pressure of water P_s is fixed at 1 atmosphere. The water source now is used as a boiler (without N_2 bubbling) which generates steam at a fixed rate set by the temperature of the hot plate surface. The steam is superheated to test temperature T in the heated conduit for steam. The hot plate that holds the sample is set to test temperature T.

Appendix B

Mapping the mechanical stress profile

Chapter 4 discusses usage of mechanical stress measurements to extract the diffusion coefficient, D, of water. The mechanical stress, $\Delta(x,t)$, as a function of depth, x, and at time, t at high temperature and relative humidity, is used to extract the diffusion coefficient. After calibration with SIMS it also can be used to map the concentration of water as a function of depth.

To map the profile $\Delta(x,t)$, we use samples with barrier layers over a range of thicknesses, and determine that the stress follows a complementary error function distribution that reflects the water distribution. Consider a system of 4 barrier layers of thicknesses $h_1 < h_2 < h_3 < h_4$ deposited on four different silicon substrates. The four barrier films are held at elevated temperatures and relative humidity to speed up water diffusion. The barriers then have mechanical stress $\sigma_1(t)$, $\sigma_2(t)$, $\sigma_3(t)$ and $\sigma_4(t)$ at time t.The average stress in the thickest barrier is the linear combination of average stress $\delta_1(t)$, $\delta_2(t)$, $\delta_3(t)$ and $\delta_4(t)$, where $\delta_1(t)$ is the average stress between depths 0 and h_1, δ_2 is the average stress between depths h_1 and h_2, and so on. Table B.1 summarizes the stress notations used in this appendix.

Table B.1: Symbols: Mechanical stress profile within a film.

$\Delta(x,t)$	Stress as a function of depth, x and time, t
$\sigma_i(t)$	Average stress between depths 0 and $h_i(t)$
$\delta_i(t)$	Average stress between depths $h_{i-1}(t)$ and $h_i(t)$

We aim to map the stress, $\Delta(x,t)$ for the thickest barrier, where,

$$\Delta(x,t) = \begin{cases} \delta_1(t), & \text{if } 0 \le x < h_1 \\ \delta_2(t), & \text{if } h_1 \le x < h_2 \\ \delta_3(t), & \text{if } h_2 \le x < h_3 \\ \delta_4(t), & \text{if } h_3 \le x \le h_4 \end{cases} \tag{B.1}$$

If the barrier material properties are identical and independent of thickness, to the first order,

$$\begin{aligned} \sigma_1(t) &= \delta_1(t) \\ \sigma_2(t) &= \frac{\delta_1(t)\,h_1 + \delta_2(t)\,(h_2 - h_1)}{h_2} \\ \sigma_3(t) &= \frac{\delta_1(t)\,h_1 + \delta_2(t)\,(h_2 - h_1) + \delta_3(t)\,(h_3 - h_2)}{h_3} \\ \sigma_4(t) &= \frac{\delta_1(t)\,h_1 + \delta_2(t)\,(h_2 - h_1) + \delta_3(t)\,(h_3 - h_2) + \delta_4(t)\,(h_4 - h_3)}{h_4} \end{aligned} \tag{B.2}$$

The linear system of equations can be rewritten as

$$\begin{pmatrix} \delta_1(t) \\ \delta_2(t) \\ \delta_3(t) \\ \delta_4(t) \end{pmatrix} = \begin{pmatrix} 1 & 0 & 0 & 0 \\ \frac{h_1}{h_2} & \frac{h_2-h_1}{h_2} & 0 & 0 \\ \frac{h_1}{h_3} & \frac{h_2-h_1}{h_3} & \frac{h_3-h_2}{h_3} & 0 \\ \frac{h_1}{h_4} & \frac{h_2-h_1}{h_4} & \frac{h_3-h_2}{h_4} & \frac{h_4-h_3}{h_4} \end{pmatrix}^{-1} \times \begin{pmatrix} \sigma_1(t) \\ \sigma_2(t) \\ \sigma_3(t) \\ \sigma_4(t) \end{pmatrix} \tag{B.3}$$

By monitoring the change in stress $\sigma_1(t)$, $\sigma_2(t)$, $\sigma_3(t)$ and $\sigma_4(t)$ for four barriers of thicknesses h_1, h_2, h_3 and h_4 respectively, we calculate $\delta_1(t)$, $\delta_2(t)$, $\delta_3(t)$ and $\delta_4(t)$ using B.3.

Expression B.1 gives the stress profile in the thickest barrier. The thinnest barrier saturates with water in short time duration. The saturated stress, $\delta_1(\infty)$, is equal to stress at the surface $\Delta(0,t)$.

Water diffuses with complementary error function distribution. Since stress, $\Delta(x,t)$, is proportional to the water concentration and the diffusing water concentration follows complementary error function, we have,

$$\Delta(x,t) = \Delta(0,t) \times erfc\left(\frac{x}{2\sqrt{Dt}}\right) \tag{B.4}$$

From equation B.4, at depth $x = \sqrt{Dt}$, we have $\Delta(x,t) = \Delta(0,t)/2$. In other words, at time t, the depth at which the stress drops to half of the surface value is determined by the diffusion coefficient and is $\sqrt{Dt}$. This depth, $L = \sqrt{Dt}$ is known as the diffusion length. By monitoring diffusion length, L, as a function of time, t, the diffusion coefficient, D is evaluated.

B.1 Experimental details

To measure the diffusion coefficient and to demonstrate that the stress profile inside a barrier layer is the same as the water concentration profile, 4 barrier films of different thicknesses were fabricated on a silicon wafer. The barrier film is deposited in the PECVD with recipe given by table 3.2.

The mechanical stress was measured as function of time for four samples $\sigma_1(t)$, $\sigma_2(t)$, $\sigma_3(t)$ and $\sigma_4(t)$ of thicknesses 159 nm, 309 nm, 873 nm and 2100 nm, respectively, after they had been held in a 100 °C boiling water bath.

B.2 Results

Using equation B.3 and B.1 the stress profile, $\Delta(x,t)$, was obtained by calculating values $\delta_1(t)$, $\delta_2(t)$, $\delta_3(t)$ and $\delta_4(t)$. The saturated stress is obtained by the saturated stress value of the thinnest sample. The stress profile is given in figure B.1. The diffusion length is defined as the depth at which the stress drops to half of its surface value. The diffusion length was found to be proportional to $\sqrt{t}$ as given in figure B.2 with diffusion coefficient of 1.3×10^{-14} cm^2/s.

The PECVD chamber is usually cleaned every 2 μm of barrier layer deposition. When this experiment was performed, the PECVD chamber had undergone over 10 μm thick barrier layer deposition. The barrier film deposited after 7 μm of prior deposition results in higher diffusion coefficient. This change in diffusion coefficient for depositions greater than 7 μm in the PECVD chamber were not known during the time of the experiment. As a result the measured diffusion coefficient 1.3×10^{-14} cm^2/s is greater than the value reported in chapter 4.

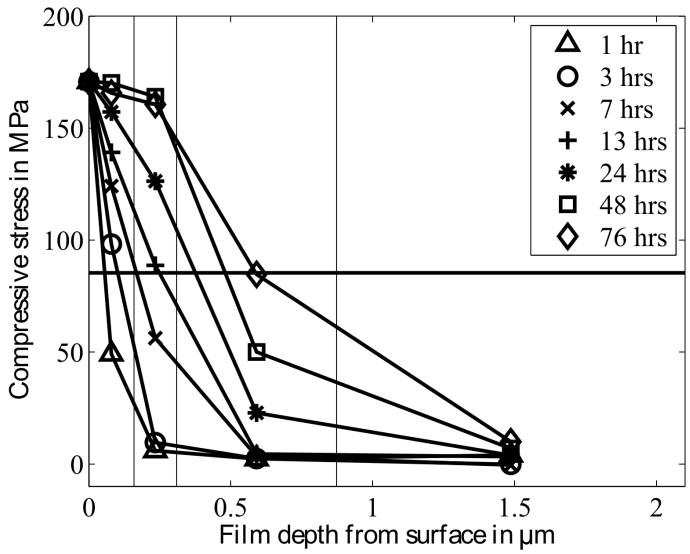

Figure B.1: Mapped stress profile in a 2.1 µm thick barrier film at different time intervals. The sample was held at the accelerated test conditions of 100 °C and 100% relative humidity.

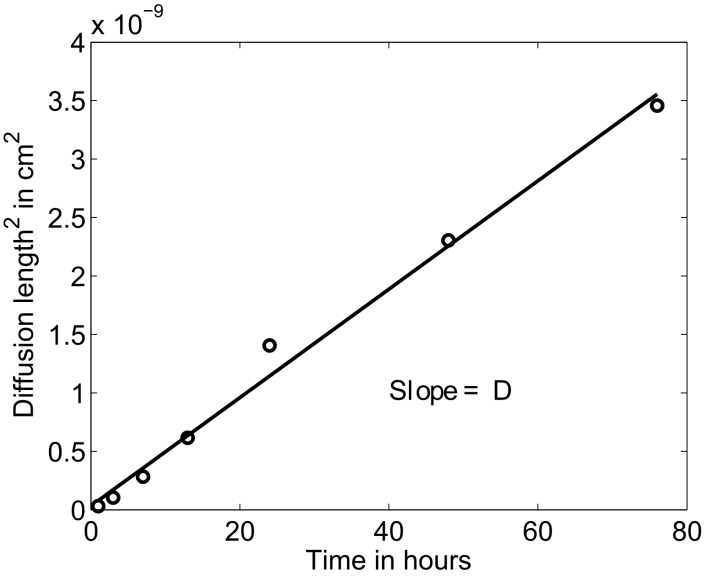

Figure B.2: The diffusion length in the sample of figure B.1 measured at time intervals given. The diffusion length is the depth from surface at which the stress drops to half the value of the stress at the surface. The diffusion coefficient is 1.3×10^{-14} cm^2/s.

Appendix C

Adding ammonia to the barrier deposition

The deposition conditions for the barrier film on which chapters 4 through 10 is given in table 3.2. The gases that are fed into the chamber during deposition are HMDSO and oxygen exclusively. To show the effect of ammonia addition on the properties of the barrier material, ammonia gas is added to the input gases, and the diffusion is measured with the mechanical stress technique described in chapter 4 and appendix B.

A 10 sccm MKS mass flow controller was used to feed the ammonia gas. Special care is taken to use neoprene instead of viton in the mass flow controller. Viton seal swells upon exposure to ammonia.

Four films were deposited on four different 100 mm diameter silicon wafer for a barrier film thickness of 1.5 μm. The ammonia flow rates of 0, 1,2 and 4 sccm respectively, were added to the input gas in the deposition four films. Figure C.1 shows the mechanical stress in an as-deposited film as a function of NH_3 flow rates.

The films were exposed to 100 °C and 100% relative humidity. All the films became more compressive. Figure C.2 gives the square of the change in stress of the 1.5 μm barrier films as a function of time. The linear behaviour of the square of the increase stress as a function of time suggests that the stress follows a complementary error function of depth and so likely does the water

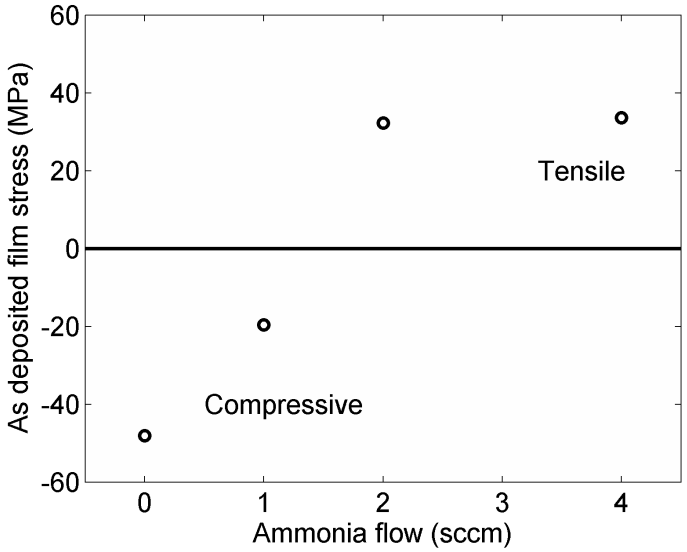

Figure C.1: Stress of as deposited barrier films as a function of ammonia flow rate. Ammonia is added to the recipe of table 3.2. Negative and positive stress correspond to compressive and tensile stress in the film respectively.

concentration. The diffusion coefficient of water in the films are evaluated from this evolution of the mechanical stress over time. It is shown in figure C.3.

The results are that the addition of ammonia makes the barrier film's mechanical stress more tensile, and increases the water diffusion coefficient in the barrier film.

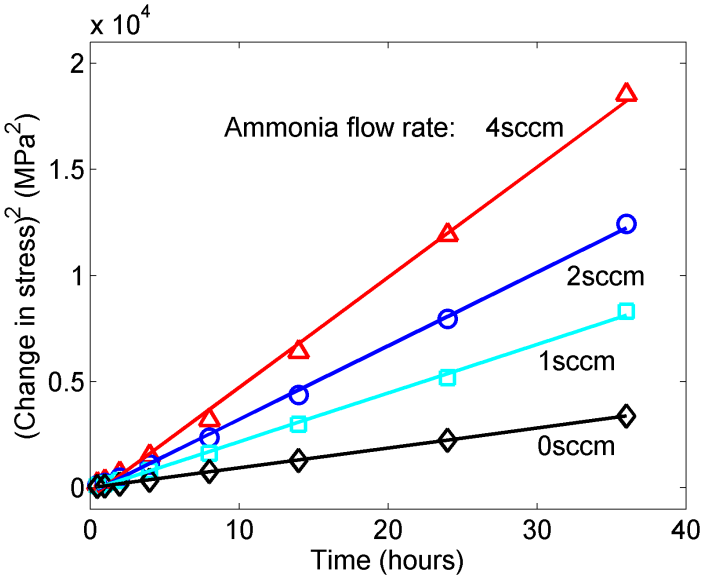

Figure C.2: Square of the change in mechanical stress in the films deposited with ammonia is plotted as a function of exposure time. Addition of ammonia results in more rapid rise of compressive stress. The markers correspond to measured data and the lines are linear best fits. From the slope of the line, the diffusion coefficient is calculated.

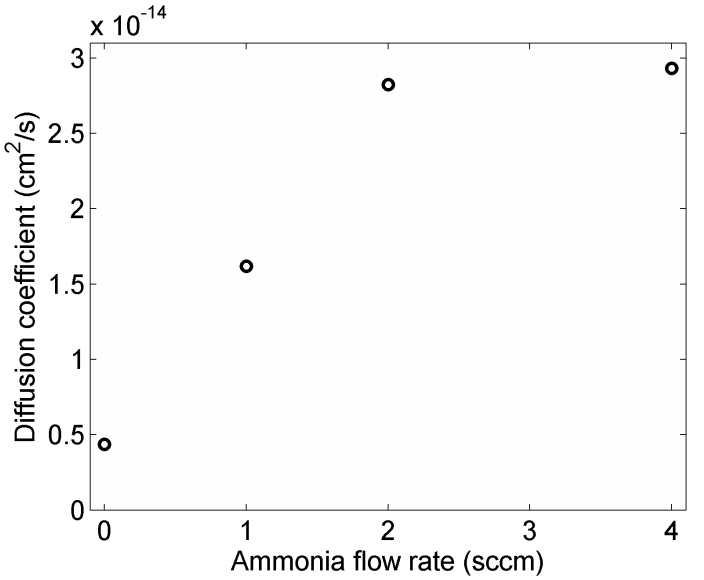

Figure C.3: Diffusion coefficient of water in the barrier films deposited with ammonia measured at 100 °C as a function of ammonia flow rate. The diffusion coefficient increases with the introduction of ammonia.

Appendix D

X-Ray diffraction of the barrier film

Grazing Incidence X-Ray Diffraction (XRD) is performed on the barrier film to find out the crystal structure, if any for the hybrid barrier film. Figure D.1 shows the result. A 938 nm thick barrier film was deposited with the recipe given in table 3.2 on a <100> oriented silicon wafer. The XRD conditions are given in table D.1. The XRD spectrum in figure D.1 shows that the barrier film is amorphous. The peak at $2\theta = 51.45°$, however, is unexplained. This peak is not associated with the barrier film, as it was observed at 51.45° in the sample with barrier film on the silicon substrate and on the bare silicon substrate.

The broad peak at 20° for barrier film on the silicon wafer suggests that the hybrid is an amorphous barrier film resembling fused silica in structure[71, 72, 73, 74]. Crystalline forms of SiO_2: quartz, cristobalite and tridymite have sharp XRD peaks between 20° and 30° which are not visible in our case[75].

The silicon substrate is a single crystal <100> wafer. The X-Ray source arrives at 1° angle from the plane of the substrate. The mounting and orientation of the wafer is described in figure D.2. The low incidence angle eliminates diffraction from the <100> substrate. This is because for

Table D.1: Grazing angle X-ray diffraction conditions.

X-Ray source	Cu Kα 1.54Å
Substrate	<100> 500 µm silicon
Barrier film thickness	938nm
Scan time	0.3 seconds/step
Scan step	0.01°

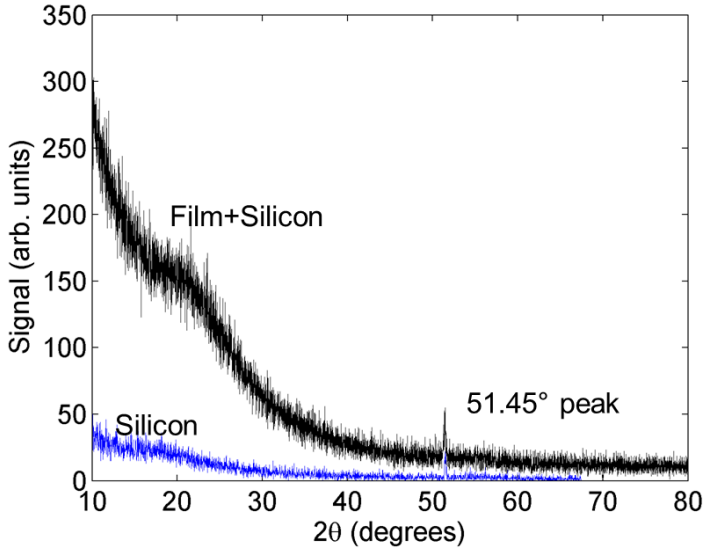

Figure D.1: Grazing angle X-ray diffraction spectra obtained from a 938 nm thick barrier film deposited on a silicon wafer, and from a bare silicon wafer. The recipe for deposition is that given in table 3.2. A single diffraction peak is observed at 51.45° in both barrier film samples, ruling out that it originates from the barrier film.

a peak to appear from a Bragg plane in the silicon wafer from Grazing Incidence XRay diffraction, two conditions need to be simultaneously satisfied. They are:

1. Bragg's law of diffraction needs to be satisfied. $n\lambda = 2dsin\,(\theta)$, where 2θ is the angle between the source and the detector.

2. The same diffracting Bragg plane should be at an angle $(\theta - 1^{\circ})$ from the (100) plane.

No Bragg plane satisfies the two criteria for the single crystal silicon mounted the way shown in figure D.2. Hence 51.45° peak can be concluded to be not from the silicon substrate. The actual cause of the peak is yet to be identified.

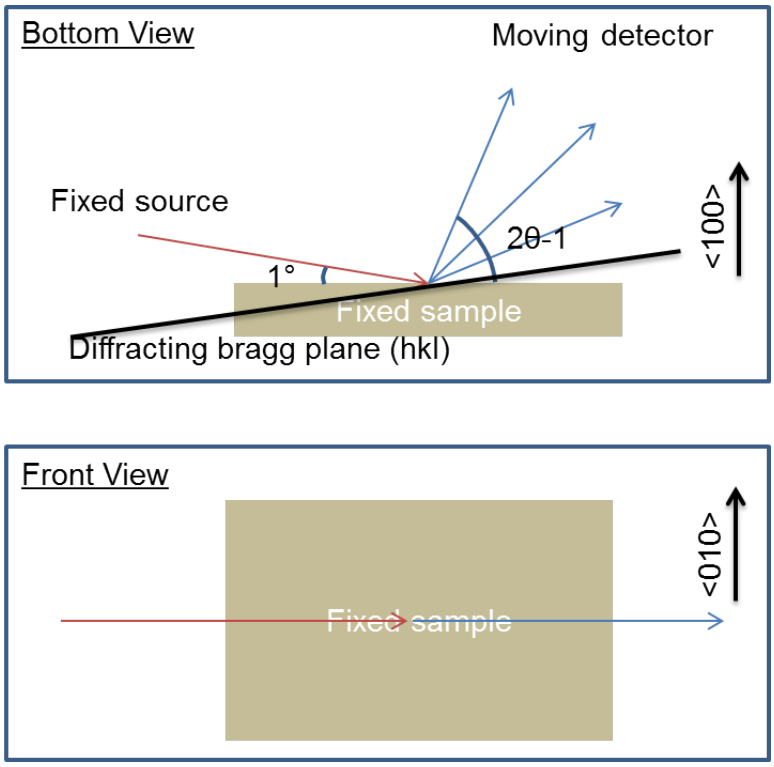

Figure D.2: Grazing angle X-Ray diffraction setup to characterize the evaluate whether the barrier material is amorphous or crystalline.

Appendix E

List of publications

E.1 Patents

3 Invention disclosures under review on encapsulation of Organic Light Emitting Diodes. (1 application published so far)

1. Mandlik. P., Ma Ruiqing., Wagner S., Lalgudi Visweswaran B., "Barrier film for electronic devices and substrates", US Patent Application US20140087497 A1, March 27, 2014.

E.2 Publications

1. Bhadri Visweswaran, Siddharth Harikrishna Mohan, Prashant Mandlik, Jeff Silvernail, Rui-Qing Ma, James Sturm and Sigurd Wagner, "Predicting the Lifetime of Flexible Permeation Barrier Layers for OLED Displays," *SID Symposium Digest of Technical Papers*, vol. 45, no. 1, pp.111-113, June 2014.

E.3 Conference talks

1. Bhadri Visweswaran, Siddharth Harikrishna Mohan, William Quinn, Jeff Silvernail, Rui-Qing Ma, James Sturm and Sigurd Wagner, "Evaluation and Lifetime Prediction of a Single-Layer Permeation Barrier Film for Flexible Organic Light Emitting Diode Displays," *Materials Research Society*, abstract: CC11.02, San Francisco, CA, April 2014.

2. Bhadri Visweswaran, Prashant Mandlik, Siddharth Harikrishna Mohan, Jeff Silvernail, Rui-Qing Ma, James Sturm and Sigurd Wagner, "Measuring the Diffusion Coefficient of Water in High Quality Permeation Barrier Layers," *American Vacuum Society*, abstract: 3146, Los Angeles, CA, October 2013.

3. Bhadri Visweswaran, Prashant Mandlik, Jeff Silvernail, Rui-Qing Ma, James Sturm and Sigurd Wagner, "Measurement and Analysis of Bulk Diffusion of Water in Permeation Barrier Layers," *Materials Research Society*, abstract: B11.87, San Francisco, CA, April 2013.

4. Bhadri Visweswaran, Lin Han, Prashant Mandlik, Jeff Silvernail, Rui-Qing Ma, James Sturm and Sigurd Wagner, "Organic LED Encapsulation with a Hybrid of SiO2 and Silicone Polymer," *Materials Research Society*, abstract: J14.10, San Francisco, CA, April 2012.

5. Bhadri Visweswaran, Lin Han, James Sturm and Sigurd Wagner, "Effect of a-Si Thickness on Performance of P-channel a-Si TFT Using a Hybrid Gate Dielectric," *Materials Research Society*, abstract A19.1., San Francisco, CA, April 2011.

Bibliography

[1] G. Gustafsson, Y. Cao, G. M. Treacy, F. Klavetter, N. Colaneri, and A. J. Heeger, "Flexible light-emitting diodes made from soluble conducting polymers," *Nature*, vol. 357, no. 6378, pp. 477–479, 1992.

[2] G. Gu, P. E. Burrows, S. Venkatesh, S. R. Forrest, and M. E. Thompson, "Vacuum-deposited, nonpolymeric flexible organic light-emitting devices," *Optics Letters*, vol. 22, no. 3, pp. 172–174, 1997.

[3] D. Kolosov, D. S. English, V. Bulovic, P. F. Barbara, S. R. Forrest, and M. E. Thompson, "Direct observation of structural changes in organic light emitting devices during degradation," *Journal of Applied Physics*, vol. 90, no. 7, pp. 3242–3247, 2001.

[4] P. E. Burrows, V. Bulovic, S. R. Forrest, L. S. Sapochak, D. M. Mccarty, and M. E. Thompson, "Reliability and degradation of organic light-emitting devices," *Applied Physics Letters*, vol. 65, no. 23, pp. 2922–2924, 1994.

[5] M. S. Weaver, L. A. Michalski, K. Rajan, M. A. Rothman, J. A. Silvernail, J. J. Brown, P. E. Burrows, G. L. Graff, M. E. Gross, P. M. Martin, M. Hall, E. Mast, C. Bonham, W. Bennett, and M. Zumhoff, "Organic light-emitting devices with extended operating lifetimes on plastic substrates," *Applied Physics Letters*, vol. 81, no. 16, pp. 2929–2931, 2002.

[6] Y. Leterrier, Y. Wyser, J. A. E. Manson, and J. Hilborn, "A method to measure the adhesion of thin glass coatings on polymer films," *The Journal of Adhesion*, vol. 44, no. 3, pp. 213–227, 1994.

[7] Y. Leterrier, "Durability of nanosized oxygen-barrier coatings on polymers," *Progress in Materials Science*, vol. 48, no. 1, pp. 1–55, 2003.

[8] A. G. Erlat, R. J. Spontak, R. P. Clarke, T. C. Robinson, P. D. Haaland, Y. Tropsha, N. G. Harvey, and E. A. Vogler, "SiOx gas barrier coatings on polymer substrates: Morphology and gas transport considerations," *Journal of Physical Chemistry B*, vol. 103, no. 29, pp. 6047–6055, 1999.

[9] Y. Leterrier, L. Boogh, J. Andersons, and J. A. E. Manson, "Adhesion of silicon oxide layers on poly(ethylene terephthalate) .1. Effect of substrate properties on coating's fragmentation process," *Journal of Polymer Science Part B-Polymer Physics*, vol. 35, no. 9, pp. 1449–1461, 1997.

[10] Y. Leterrier, J. Andersons, Y. Pitton, and J. A. E. Manson, "Adhesion of silicon oxide layers on poly(ethylene terephthalate) .2. Effect of coating thickness on adhesive and cohesive strengths," *Journal of Polymer Science Part B-Polymer Physics*, vol. 35, no. 9, pp. 1463–1472, 1997.

[11] J. Affinito, "Environmental barrier material for organic light emitting device and method of making," Jul. 31 2001, US Patent 6,268,695.

[12] T. Harvey, S. Shi, and F. So, "Hermetic sealing of plastic substrate," 1997, US Patent 5,686,360.

[13] A. B. Chwang, M. A. Rothman, S. Y. Mao, R. H. Hewitt, M. S. Weaver, J. A. Silvernail, K. Rajan, M. Hack, J. J. Brown, X. Chu, L. Moro, T. Krajewski, and N. Rutherford, "Thin film encapsulated flexible organic electroluminescent displays," *Applied Physics Letters*, vol. 83, no. 3, pp. 413–415, 2003.

[14] G. L. Graff, R. E. Williford, and P. E. Burrows, "Mechanisms of vapor permeation through multilayer barrier films: Lag time versus equilibrium permeation," *Journal of Applied Physics*, vol. 96, no. 4, pp. 1840–1849, 2004.

[15] P. Mandlik, J. Gartside, L. Han, I. C. Cheng, S. Wagner, J. A. Silvernail, R. Q. Ma, M. Hack, and J. J. Brown, "A single-layer permeation barrier for organic light-emitting displays," *Applied Physics Letters*, vol. 92, no. 10, p. 103309, 2008.

[16] L. Han, P. Mandlik, J. Gartside, S. Wagner, J. A. Silvernail, R. Q. Ma, M. Hack, and J. J. Brown, "Properties of a permeation barrier material deposited from hexamethyl disiloxane and oxygen," *Journal of the Electrochemical Society*, vol. 156, no. 2, pp. H106–H114, 2009.

[17] Y. F. Liew, H. Aziz, N. X. Hu, H. S. O. Chan, G. Xu, and Z. Popovic, "Investigation of the sites of dark spots in organic light-emitting devices," *Applied Physics Letters*, vol. 77, no. 17, p. 2650, 2000.

[18] F. Papadimitrakopoulos, X.-M. Zhang, and K. A. Higginson, "Chemical and morphological stability of aluminum tris (8-hydroxyquinoline)(AlQ3): effects in light-emitting devices," *IEEE Journal of Selected Topics in Quantum Electronics*, vol. 4, no. 1, pp. 49–57, 1998.

[19] P. E. Burrows, G. L. Graff, M. E. Gross, P. M. Martin, M. K. Shi, M. Hall, E. Mast, C. Bonham, W. Bennett, and M. B. Sullivan, "Ultra barrier flexible substrates for flat panel displays," *Displays*, vol. 22, no. 2, pp. 65–69, 2001.

[20] E. Lueder, "Passive and active matrix liquid crystal displays with plastic substrates," in *Proceedings of the fourth symposium on Thin film transistor technologies*, vol. 98. Boston, MA: The Electrochemical Society, 1999, pp. 336–354.

[21] J. Y. Kim, D. Sohn, and E. R. Kim, "Polymer-based multi-layer conductive electrode film for plastic lcd applications," *Applied Physics A*, vol. 72, no. 6, pp. 699–704, 2001.

[22] H. Chatham, "Oxygen diffusion barrier properties of transparent oxide coatings on polymeric substrates," *Surface and Coatings Technology*, vol. 78, no. 1-3, pp. 1–9, 1996.

[23] J. S. Park, H. Chae, H. K. Chung, and S. I. Lee, "Thin film encapsulation for flexible am-oled: a review," *Semiconductor Science and Technology*, vol. 26, no. 3, p. 034001, 2011.

[24] P. Mandlik, "A novel hybrid inorganic-organic single layer barrier for organic light emitting diodes," Ph.D. dissertation, Princeton University, January 2009.

[25] P. Mandlik, L. Han, S. Wagner, J. A. Silvernail, R. Q. Ma, M. Hack, and J. J. Brown, "Diffusion of atmospheric gases into barrier-layer sealed organic light emitting diodes," *Applied Physics Letters*, vol. 93, no. 20, p. 042111, 2008.

[26] R. S. Kumar, M. Auch, E. Ou, G. Ewald, and C. Soo Jin, "Low moisture permeation measurement through polymer substrates for organic light emitting devices," in *Proceedings of the International Conference on Materials for Advanced Technologies (ICMAT-2001)Symposium G: Plastic Electronics - Materials and Devices*, vol. 417, no. 12, Singapore, 2002, pp. 120 – 126.

[27] R. L. Hamilton, "Water vapor permeability of polyethylene and other plastic materials," *Bell System Technical Journal*, vol. 46, no. 2, p. 391, 1967.

[28] G. Graff, P. Martin, M. Gross, M. Shi, M. Hall, and E. Mast, "Semicoductor passivation using barrier coatings," Apr. 15 2003, US Patent 6,548,912.

[29] G. Graff, M. Gross, M. Shi, M. Hall, P. Martin, and E. Mast, "Ultrabarrier substrates," Jul. 2 2002, US Patent 6,413,645.

[30] G. Graff, M. Gross, J. Affinito, M. Shi, M. Hall, and E. Mast, "Environmental barrier material for organic light emitting device and method of making," Feb. 18 2003, US Patent 6,522,067.

[31] M. Schaepkens and K. Flanagan, "An organic electroluminescent devices having a flexible, radiation-transparent substrate coated with a protective coating of an inorganic and an organic material of varing thickness to resist diffusion of moisture and oxygen; comprises an electrode pair and a sandwiched organic light-emitting layer," Mar. 21 2006, US Patent 7,015,640.

[32] T. N. Chen, D. S. Wuu, C. C. Wu, R. H. Horng, H. F. Wei, L. Y. Jiang, H. U. Lee, and Y. Y. Chang, "Deposition and characterization of ultra-high barrier coatings for flexible electronic applications," *Vacuum*, vol. 84, no. 12, pp. 1444–1447, 2010.

[33] ASTM Standard F1249 - 13, 2013, "Standard test method for water vapor transmission rate through plastic film and sheeting using a modulated infrared sensor."

[34] R. Dunkel, R. Bujas, A. Klein, and V. Horndt, "Method of measuring ultralow water vapor permeation for oled displays," *Proceedings of the IEEE*, vol. 93, no. 8, pp. 1478–1482, Aug 2005.

[35] M. D. Groner, S. M. George, R. S. McLean, and P. F. Carcia, "Gas diffusion barriers on polymers using Al2O3 atomic layer deposition," *Applied Physics Letters*, vol. 88, no. 5, p. 051907, 2006.

[36] J. H. Choi, Y. M. Kim, Y. W. Park, J. W. Huh, B. K. Ju, I. S. Kim, and H. N. Hwang, "Evaluation of gas permeation barrier properties using electrical measurements of calcium degradation," *Review of Scientific Instruments*, vol. 78, no. 6, p. 064701, 2007.

[37] R. Paetzold, A. Winnacker, D. Henseler, V. Cesari, and K. Heuser, "Permeation rate measurements by electrical analysis of calcium corrosion," *Review of Scientific Instruments*, vol. 74, no. 12, pp. 5147–5150, 2003.

[38] M. Creatore, F. Palumbo, D'Agostino, and P. Fayet, "Rf plasma deposition of sio2-like films: plasma phase diagnostics and gas barrier film properties," *Surface Coating Technology*, vol. 142-144, pp. 163–168, 2001.

[39] H. Yasuda, "Plasma polymerization for protective coatings and composite membranes," *Journal of Membrane Science*, vol. 18, pp. 273–284, 1984.

[40] A. M. Wrobel and M. R. Wertheimer, *Plasma-Polymerized Organosilicones and Organomettalics in Plasma Deposition, Treatment and Etching of Polymers.* New York: Academic Press Inc., 1990.

[41] H. Biederman and Y. Osada, *Plasma Polymerization Processes.* New York: Elsevier, 1992.

[42] R. Hora and C. Wohlrab, "Plasma polymerization: A new technology for functional coatings on plastics," in *36th Annual Technical Conference.* Proceedings of the Society of Vacuum Coaters, 1993, pp. 51–55.

[43] H. Grunwald, R. Adam, J. Bartella, M. Jung, W. Dicken, S. Kunkel, K. Nauenburg, T. Gebele, S. Mitzlaff, G. Ickes, U. Patz, and J. Snyder, "Better aluminum mirrors by integrating plasma pretreatment, sputtering and plasma polymerization of large-scale car headlight production," *Surface Coating Technology*, vol. 111, pp. 287–296, 1999.

[44] J. T. Felts and A. D. Grubb, "Commercial-scale application of plasma processing for polymeric substrate: From laboratory to production," *Journal of Vacuum Science & Technology*, vol. A, no. 10, pp. 1675–1681, 1992.

[45] A. J. Beck, F. R. Jones, and R. D. Short, "Mass spectrometric study of the radiofrequency-induced plasma polymerization of styrene and propenoic acid," *Journal of the Chemical Society, Faraday Transactions*, vol. 94, pp. 559–565, 1998.

[46] L. Han, "A new SiO2-silicone hybrid insulator for amorphous silicon thin film transistors," Ph.D. dissertation, Princeton University, May 2011.

[47] J. Weichart and J. Muller, "Plasma polymerization of silicon organic membranes for gas separation," *Journal of Surface Coatings and Technology*, vol. 59, pp. 342–344, 1993.

[48] K. Aumaille, C. Vallee, A. Granier, A. Goullet, F. Gaboriau, and G. Turban, "A comparative study of oxygen/organosilicon plasmas and thin sioxcyhz films deposited on helicon reactor," *Thin Solid Films*, vol. 359, pp. 188–196, 2000.

[49] H. U. Poll, J. Meichsner, M. Arzt, M. Friedrich, R. Rochotzki, and E. Kreyxig, "Optical properties of plasma polymer films," *Journal of Surface Coatings and Technology*, vol. 59, pp. 365–370, 1993.

[50] R. Basner, R. Foest, M. Schmidt, K. Backer, and H. Deutsch, "Absolute total and partial electron impact ionization cross sections of hexamethydisiloxane," *International Journal of Mass Spectrometry*, vol. 176, pp. 245–252, 1998.

[51] E. Kny, L. L. Levenson, W. J. James, and R. A. Auerbach, "Interface composition and adhesion of glow-discharge-formed organo-tin polymers," *Journal of Vacuum Science & Technology*, vol. 16, pp. 359–362, 1979.

[52] J. A. Theil, J. G. Brace, and R. W. Knoll, "Carbon content of silicon oxide films deposited by room temperature plasma enhanced chemical vapor deposition of hexamethyldisiloxane and oxygen," *Journal of Vacuum Science & Technology A*, vol. 12, no. 4, pp. 1365–1370, 1994.

[53] G. Tochitani, M. Shimozuma, and H. Tagashira, "depositions of silicon oxide films from teos by low frequency plasma chemical vapor deposition," *Journal of Vacuum Science & Technology*, vol. A11, pp. 400–405, 1993.

[54] H. Li, A. Belkind, F. Jansen, and Z. Orban, "an in situ xps study of oxygen plasma cleaning of aluminum surfaces," *Journal of Surface Coatings and Technology*, vol. 92, pp. 171–177, 1997.

[55] R. H. Doremus, "Diffusion of water in silica glass," *Journal of Materials Research*, vol. 10, no. 9, pp. 2379–2389, 1995.

[56] J. Crank, *The mathematics of diffusion*, 2nd ed. Oxford, Eng: Clarendon Press, 1975.

[57] J. Fraden, "Handbook of modern sensors: Physics, designs, and applications, fourth edition," *Handbook of Modern Sensors: Physics, Designs, and Applications, Fourth Edition*, p. 445, 2010.

[58] L. D. Landau and E. M. Lifshits, *Electrodynamics of continuous media*. Pergamon Press, 1960, vol. 8.

[59] L. Hartshorn, N. J. L. Megson, and E. Rushton, "The structure and electrical properties of protective films," *Journal of the society of Chemical Industy*, vol. 56, p. 266T, 1937.

[60] G. G. Stoney, "The tension of metallic films deposited by electrolysis," *Proceedings of the Royal Society of London Series a-Containing Papers of a Mathematical and Physical Character*, vol. 82, no. 553, pp. 172–175, 1909.

[61] K. M. Davis and M. Tomozawa, "Water diffusion into silica glass - structural-changes in silica glass and their effect on water solubility and diffusivity," *Journal of Non-Crystalline Solids*, vol. 185, no. 3, pp. 203–220, 1995.

[62] R. H. Doremus, "Diffusion of water in crystalline and glassy oxides: Diffusion-reaction model," *Journal of Materials Research*, vol. 14, no. 9, pp. 3754–3758, 1999.

[63] C. Y. Chang, J. McVittie, J. Li, K. Saraswat, S. Lassig, and J. Dong, "Profile simulation of plasma enhanced and ECR oxide deposition with sputtering," in *International Electron Devices Meeting, 1993. Technical Digest*, Washington, DC, USA, Dec 1993, pp. 853–856.

[64] J. McVittie, J. Rey, L. Cheng, M. IslamRaja, and K. Saraswat, "LPCVD profile simulation using a re-emission model," in *International Electron Devices Meeting, 1990. Technical Digest*, San Francisco, CA, USA, Dec 1990, pp. 917–920.

[65] Y. Yang, S. Jayaraman, G. S. Girolami, D. Y. Kim, and J. R. Abelson, "cvd growth kinetics of hfb2 thin films from the single source precursor hf(bh4)4," *Chem. Mater.*, vol. 18, p. 5088, 2006.

[66] A. Yanguas-Gil, Y. Yang, N. Kumar, and J. R. Abelson, "Highly conformal film growth by chemical vapor deposition. a conformal zone diagram based on kinetics," *Journal of Vacuum Science & Technology*, vol. A 27(5), pp. 1235–1243, 2009.

[67] R. Robertson and A. Gallagher, "Reaction mechanism and kinetics of silane pyrolysis on a hydrogenated amorphous silicon surface," *Journal of Chemical Physics*, vol. 85, p. 3623, 1986.

[68] J. C. Rey, L. Cheng, J. P. McVittei, and K. C. Saraswat, "monte carlo low pressure deposition profile simulations," *Journal of Vacuum Science & Technology*, vol. A 9(3), pp. 1083–1087, 1990.

[69] T. S. Cale, G. B. Raupp, and T. H. Gandy, "Ballistic transportreaction prediction of film conformality in tetraethoxysilane O2 plasma enhanced deposition of silicon dioxide," *Journal of Vacuum Science & Technology A*, vol. 10, no. 4, pp. 1128–1134, 1992.

[70] J. A. Theil, "Sticking Probability and Step Coverage Studies of SiO2 and Polymerized Siloxane Thin Films Deposited by Plasma Enhanced Chemical Vapor Deposition," in *MRS Proceedings*, vol. 385. Cambridge Univ Press, 1995, p. 97.

[71] "Preparation and photoluminescence of nanocrystalline Si-rich silicon oxide films by PECVD," *Materials Letters*, vol. 61, no. 2, pp. 463 – 465, 2007.

[72] L. Dai, X. L. Chen, T. Zhou, and B. Q. Hu, "Aligned silica nanofibres," *Journal of Physics: Condensed Matter*, vol. 14, no. 25, p. L473, 2002.

[73] T. Yordanova, P. Vasileva, I. Karadjova, and D. Nihtianova, "Submicron silica spheres decorated with silver nanoparticles as a new effective sorbent for inorganic mercury in surface waters," *Analyst*, vol. 139, pp. 1532–1540, 2014.

[74] X. Chen, J. Jiang, F. Yan, S. Tian, and K. Li, "A novel low temperature vapor phase hydrolysis method for the production of nano-structured silica materials using silicon tetrachloride," *RSC Advances*, vol. 4, pp. 8703–8710, 2014.

[75] R. T. Down, "The RRUFF Project: An integrated study of the chemistry, crystallography, raman and infrared spectroscopy of minerals," in *Program and Abstracts of the 19th General Meeting of the International Mineralogical Association*, Kobe, Japan, 2006.